

Appendix A: Supplementary Online Material

A.1

Measuring the Three-Dimensional Wind Vector Using a Five-Hole Probe

Five-hole air velocity probes (FHPs) do not provide very high temporal resolution (e.g., compared to a constant temperature anemometer (CTA)) but are robust instruments that can be easily deiced, allowing measurements up to about 100 Hz. The limit of temporal resolution is mainly due to limited response time of the connected pressure transducers and resonance effects in the connection tubes and in the cavities of the pressure transducers.

The following description mainly addresses FHPs that measure (in addition to the static air pressure) only differential pressures (Lemonis *et al.*, 2002). In larger probes (e.g., pressure holes in the aircraft fuselage as applied to the space shuttle or the F-18 High-Angle-of-Attack Research Vehicle), the measurement of the individual absolute pressures is possible and allows an even more accurate determination of the flow angles (Weiß and Leißling, 2001; Weiß 2002). Airflow systems involving more or less than five holes (Crawford and Dobosy, 1992; Sumner 2000; Pfau *et al.*, 2002) can be treated more or less like a FHP.

The local wind vector in the aircraft coordinate system is determined from the dynamic pressure increment Δp_q and the pressure differences between opposite pressure holes in the FHP, that is, the pressure difference in the horizontal plane, $\Delta p_\beta = p_4 - p_2$, and in the vertical plane, $\Delta p_\alpha = p_1 - p_3$, where p_j denotes the individual holes of the FHP, with p_5 being pressure at the central hole (Figure 2.14). The pressure differences Δp_α and Δp_β increase when the angles of attack α and sideslip β increase. But the pressure differences also depend on the airspeed (and therefore on both the dynamic pressure Δp_q and the Mach number) and on the air density ρ (and therefore on the altitude z). In general, this can be expressed by

$$\varphi = f(\Delta p_\varphi, \Delta p_q, z) \quad \text{where } \varphi = \alpha, \beta, \dots \quad (\text{A.1})$$

f denotes a functional relation.

Usually, both the influence of the airspeed and the altitude can be considered by weighting the pressure difference with the dynamic pressure increment. The most

simple assumption is then

$$\varphi = \frac{1}{K_{\text{FHP}}} \cdot \frac{\Delta p_\varphi}{\Delta p_q} \quad (\text{A.2})$$

where the calibration coefficient K_{FHP} considers any disturbance of the airstream by the FHP (and also by the entire aircraft fuselage) and local stream effects directly at the pressure hole.

Actually, the most difficult task is the determination of the dynamic pressure Δp_q (or the total pressure p_{tot}) because the stagnation point is usually located somewhere between the holes of the FHP and therefore cannot be directly measured. The approximation of the total pressure by the measured pressure p_5 at the central hole of the FHP would lead to a wind vector measurement that is very sensitive to the aircraft attitude, wind speed, and wind direction (Schlienger *et al.*, 2002) and provides only minimal accuracy.

In the following, some more sophisticated methods to estimate the correct angles of sideslip and attack are introduced (Bange, 2009). It is understood that any offset angle α_o or β_o due to bias in the pressure transducers or asymmetry of the FHP has to be quantified earlier in a laboratory, a wind tunnel, or in-flight tests. Calibration routines, both for wind tunnel experiments and flight maneuvers, can be found in the literature: Haering (1990); Wörrlein (1990); Haering (1995); Barrick *et al.* (1996); Friehe *et al.* (1996); Khelif *et al.* (1999); Weiß *et al.* (1999); Williams and Marcotte (2000); van den Kroonenberg *et al.* (2008); van den Kroonenberg (2009).

A.1.1

Rosemount Method

Given an additional pressure difference measurement

$$\Delta p_{\text{ref}} = p_5 - p_2 \quad (\text{A.3})$$

between one of the horizontal holes and the central hole (Rosemount method), the dynamic pressure increment is estimated by

$$\Delta p_q \approx \Delta p_{\text{ref}} + \frac{1}{2} \Delta p_\beta \quad (\text{A.4})$$

The flow angles are determined by Eq. (A.2) with K_{FHP} set to 0.088 for airspeeds below 0.6 Ma (Rosemount, 1982). There is a different K for Eq. (A.2) and Eq. (A.4): Rosemount method 2, Eq. (A.2): $K = 0.078$, and Rosemount method 1, Eq. (A.4): $K = 0.088$. It has to be noted that Δp_{ref} refers only to the horizontal plane, that is, the stagnation point is assumed to be located somewhere on the connecting line between the two opposite holes #2 and #4. This presupposes two items:

- (i) the FHP has to be mounted on the aircraft in a way that $\alpha = 0$ in the absence of vertical wind ($w = 0$) and
- (ii) the aircraft is not allowed to perform larger changes in both pitch Θ or roll Φ angles; that is, this method is not suitable for highly dynamic systems.

An improvement requires an additional differential pressure measurement between the central hole and one of the holes in the vertical plane (#1 or #3), resulting in two disjunction equations of type Eq. (A.2):

$$\alpha = \frac{1}{K_{\text{FHP},\alpha}} \cdot \frac{\Delta p_\alpha}{\Delta p_{\text{ref},\alpha} + \frac{1}{2}\Delta p_\alpha} \quad (\text{A.5})$$

$$\beta = \frac{1}{K_{\text{FHP},\beta}} \cdot \frac{\Delta p_\beta}{\Delta p_{\text{ref},\beta} + \frac{1}{2}\Delta p_\beta} \quad (\text{A.6})$$

It is obvious that this method represents no fundamental improvement compared to the usual Rosemount method, as no consistent dynamic pressure increment can be determined.

A.1.2

Five-Difference Method and Calibration

More accurate results can be achieved using five pressure difference measurements: the difference between the central hole and each of the four remaining total pressure ports (Δp_{01} , Δp_{02} , Δp_{03} , Δp_{04}), and the difference between the static air pressure and the central hole (Δp_{0s}). These measurements are used to determine a total pressure difference

$$\Delta p = \left[\frac{1}{5} \sum_{i=0}^4 4 \cdot \left(p_i - \frac{1}{5} \sum_{j=0}^4 4p_j \right)^2 \right]^{\frac{1}{2}} + \left[p_0 - \frac{1}{4} \sum_{i=1}^4 4p_i \right] \quad (\text{A.7})$$

which uses the absolute pressures. Since the measurement of the absolute pressures P_i is often not feasible, Eq. (A.7) can also be expressed by the pressure differences van den Kroonenberg *et al.* (2008):

$$\begin{aligned} \Delta p = & \left\{ \frac{1}{125} \left[(\Delta p_{01} + \Delta p_{02} + \Delta p_{03} + \Delta p_{04})^2 + (-4\Delta p_{01} + \Delta p_{02} + \Delta p_{03} + \Delta p_{04})^2 \right. \right. \\ & + (\Delta p_{01} - 4\Delta p_{02} + \Delta p_{03} + \Delta p_{04})^2 + (\Delta p_{01} + \Delta p_{02} - 4\Delta p_{03} + \Delta p_{04})^2 \\ & \left. \left. + (\Delta p_{01} + \Delta p_{02} + \Delta p_{03} - 4\Delta p_{04})^2 \right] \right\}^{0.5} \\ & + \frac{1}{4} (\Delta p_{01} + \Delta p_{02} + \Delta p_{03} + \Delta p_{04}) \end{aligned} \quad (\text{A.8})$$

Next step is to calculate the dimensionless pressure coefficients

$$k_\alpha = \frac{\Delta p_{01} - \Delta p_{03}}{\Delta p} \quad (\text{A.9})$$

$$k_\beta = \frac{\Delta p_{02} - \Delta p_{04}}{\Delta p} \quad (\text{A.10})$$

Then, three functions are defined to calculate the airflow angles and the dimensionless coefficient k_q (later needed for the dynamic pressure)

$$\begin{aligned} \alpha &= f_1(k_\alpha, k_\beta) \\ \beta &= f_2(k_\alpha, k_\beta) \\ k_q &= f_3(k_\alpha, k_\beta) \end{aligned} \quad (\text{A.11})$$

with the general calibration polynomial form (Bohn and Simon, 1975) with $x = \alpha, \beta, q$ and typically $m = n = 10$

$$f_x(k_\alpha, k_\beta) = \sum_{i=0}^m (k_\alpha)^i \cdot \left[\sum_{j=0}^n X_{ij} \cdot (k_\beta)^j \right] \quad (\text{A.12})$$

Here, X_{ij} represents the individual calibration tensors for the angles of attack a_{ij} (f_α) and sideslip b_{ij} (f_β) and for the dynamic pressure q_{ij} (f_q). Thus, the function (A.12) contains $m \times n$ unknown coefficients X_{ij} that have to be determined via a system of $m \times n$ independent equations (e.g., using a least squares method). The most accurate method to obtain these equations is measurements in a calibrated wind tunnel. Combinations of differential pressures with adjusted $x = \alpha, \beta, q$ can be achieved by varying the airspeed and flow angles by turning the FHP in the wind tunnel. Preferably, the FHP is mounted on the aircraft (and not be removed between calibration and measurement flight). Of course, this is only feasible for very small aircraft such as Unmanned Aerial Vehicle (UAV) and large wind tunnels. Finally, the dynamic pressure q is given by

$$q = \Delta p_{0s} + \Delta p \cdot k_q \quad (\text{A.13})$$

A.1.3

In-Flight Calibration

A.1.3.1 The Lenschow Maneuvers

Regardless of where the airflow sensors are located on the aircraft and how carefully they are calibrated, errors are likely to be present in their measured outputs. Ground tests are not useful for calculating velocity-related errors. Wind tunnel tests are difficult and prohibitively expensive for exact simulation of flight conditions. Therefore, in-flight calibrations play an important role in estimating errors and correcting aircraft measurements.

Because of the airflow distortion ahead of the aircraft, the airflow angles (attack α and sideslip β) and airspeed U measured at the aircraft nose or the tip of a nose boom may differ considerably from the actual values that would be measured far away from the aircraft (Crawford *et al.*, 1996). The airflow distortion affects not only the sensitivity but also the zero offset of angle measurements, which, therefore, must also be determined from in-flight calibrations.

Maneuvers used for this purpose involve changes in U and attitude angles. The following list summarizes several maneuvers used on NCAR aircraft equipped with an Inertial Navigation System (INS) and the information that can be obtained from them; examples of these maneuvers are shown in Figures A.1 and A.2 (Lenschow and Spyers–Duran 1989).

A.1.3.2 Reverse Heading Maneuver

Fly at constant altitude and heading (usually in smooth air above the boundary layer) for several minutes. Then turn 180° by first turning 90° in one direction,

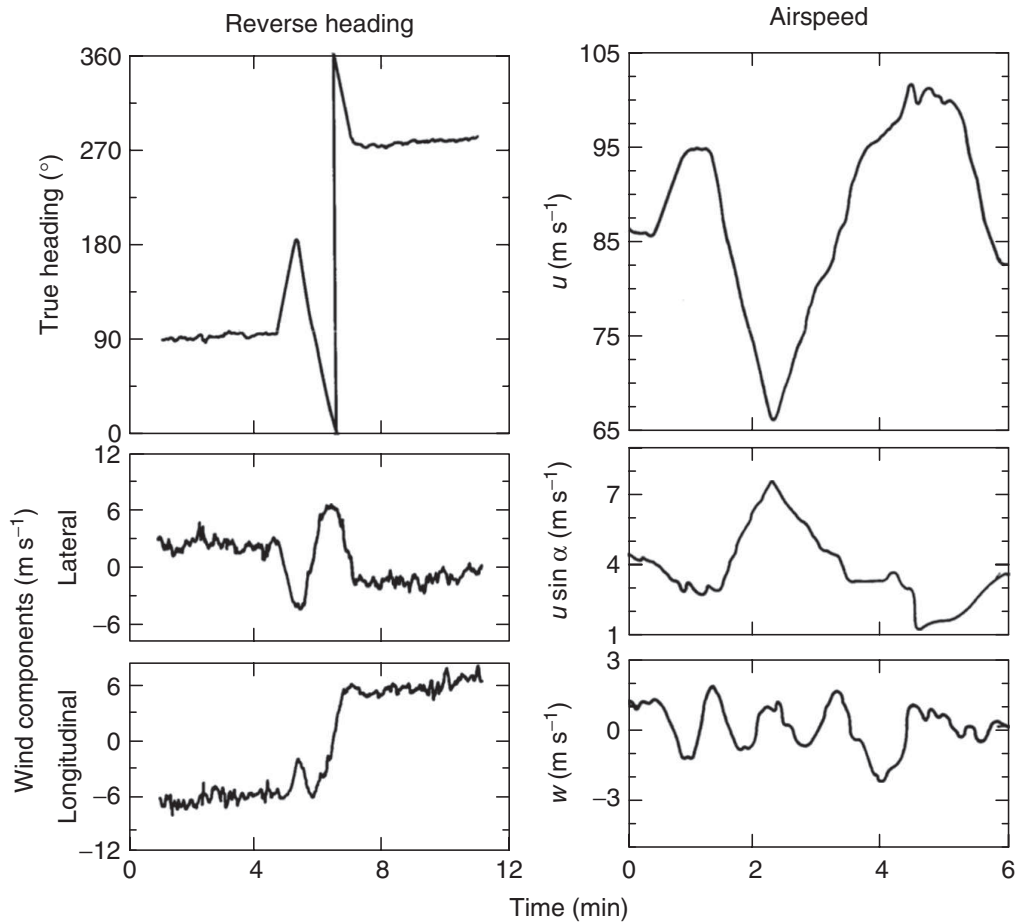


Figure A.1 Examples of reverse heading and airspeed maneuvers used to check the quality of air velocity measurements. The lateral and longitudinal velocity components are measured with respect to the aircraft; therefore, the measured wind should change sign, but not amplitude, after the 180° turn, if the wind field remains constant and is measured without error. An error in airspeed will result in a difference in the amplitude of only the longitudinal component before and after the turn, while an error in the sideslip angle will similarly affect only the lateral component, which simplifies correction procedures.

The airspeed maneuver modulates α and θ ; if θ is measured accurately, the error in α can be determined by comparing the vertical wind component with respect to the aircraft ($u \sin \alpha$) and the vertical wind component with respect to the Earth. In this example, there is little correlation between the two, so the fluctuations in w are presumed to be due to turbulence rather than an inaccurate measurement of α . The airspeed maneuver can also be used to estimate airspeed-dependent errors in other variables and the temperature recovery factor. (From Lenschow and Spyers–Duran, 1989.)

then 270° in the other direction at a constant rate so the aircraft flies through the same volume of air on its return track. This maneuver modulates errors in U and β , as they are measured in the aircraft coordinate system. The INS errors are not modulated, however, since they are measured in an inertial frame of reference. If the wind along the flight track is assumed to stay constant during this maneuver, differences in the two wind components between the two headings can be used to independently estimate errors in both U and β . U errors are associated with the longitudinal wind component; β errors, with the lateral wind component.

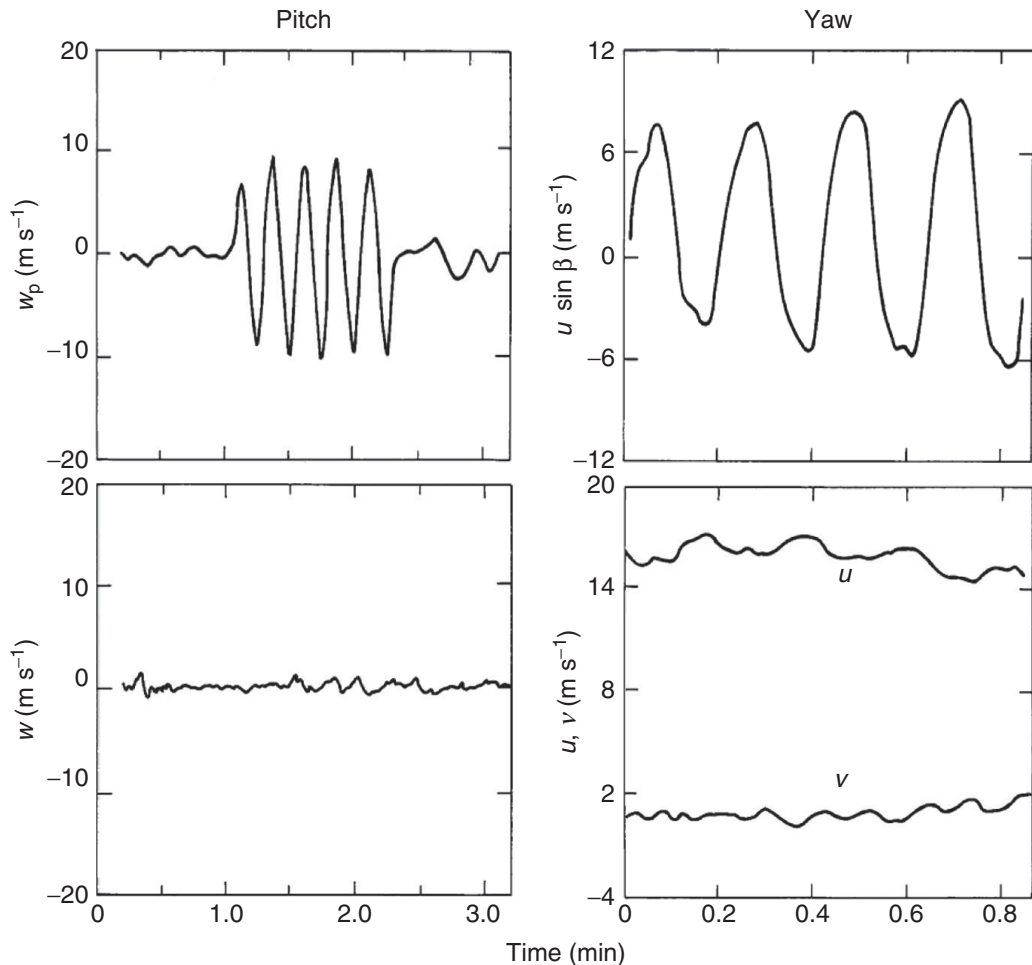


Figure A.2 Examples of pitch and yaw maneuvers. The pitch maneuver is used as an overall check on the accuracy of the w measurement; in this example, there is little modulation of w during the pitching maneuver, which implies that fluctuations in w are measured accurately. Similarly, the

yaw maneuver is used as an overall check on the lateral (with respect to the aircraft) component; again there is little modulation of u and v (in geographic coordinates) by the yawing maneuver. (From Lenschow and Spyers–Duran, 1989.)

A.1.3.3 Speed Variation Maneuver

Fly at constant altitude and heading ψ , and smoothly vary U from close to stall to close to maximum cruise speed. Since the lifting force on the aircraft is directly proportional to α and U^2 , modulating U also modulates α . For level flight, the vertical aircraft velocity w_p is zero; if the air velocity w is small, $\alpha = \theta$. Thus, α can be calibrated in flight by this technique, provided θ is measured accurately. The attitude angle transducers, in contrast to airflow angle sensors, can be accurately calibrated in the laboratory.

If U is measured incorrectly, temperature may also be affected. Temperature recovery factors can also be measured or corrected with this maneuver, as U variations modulate the measured temperature because of dynamic heating effects. Any other measurements affected by either U or α variations are also modulated by this maneuver.

A.1.3.4 Pitch Maneuver

Vary the aircraft elevator angle while holding the heading constant to obtain a sinusoidal pitching motion with a period of 10–20 s and a maximum rate of ascent and descent of $2.5\text{--}4\text{ m s}^{-1}$. This maneuver modulates w_p , U , and, to a lesser extent, α . If any of these variables have significant errors, a periodic error in w should be evident. Since the terms do not have the same phase angle, in practice, it is often possible to determine which of the variables are in error simply by determining the phase of the error in w and comparing it with the phase of w_p , θ , U , and α . This maneuver can also be used to detect dynamic errors in static air pressure or rate-of-climb instruments by comparing their outputs with the integrated INS vertical acceleration.

A.1.3.5 Yaw Maneuver

Vary the aircraft rudder angle while holding the roll and altitude constant to obtain a sinusoidal skidding or sideslip motion with a period of about 10 s and a maximum amplitude in β of about 2° . This maneuver modulates heading ψ , the longitudinal and lateral aircraft velocity components u_p and v_p , and β . As with the pitch maneuver, errors in any of these variables cause a periodic variation in the horizontal wind velocity.

On the NCAR aircraft, the system performance is judged to be satisfactory if the w error is $\leq 10\%$ of w_p for the pitch maneuver and if v_p is $\leq 10\%$ of $U \sin \beta$ for the yaw maneuver.

Lenschow and Spyers–Duran (1989) estimate that short-term (i.e., not including long-term INS drift) velocity errors can be reduced to $< 0.3\text{ m s}^{-1}$ by in-flight calibrations. An alternative technique for estimating the error coefficients in w , proposed by Khelif *et al.* (1999), is to iteratively vary the calibration coefficients of w to minimize the variance of w . This assumes that errors in the w measurement invariably increase the w variance. An advantage of this technique is that it can be done on research legs, without the requirement of dedicated maneuvers in nonturbulent air.

A.1.3.6 Rodi Maneuvers

An alternative approach developed at the University of Wyoming uses multiple regression analysis of data collected while maneuvering the aircraft in a standard rate turn. When turning, the pilot induces sinusoidal sideslip variations of about 10 s period while maintaining constant altitude, resulting in sinusoidal flow angle and airspeed variation along both the lateral and vertical body axes. The motivation for the turning method is to induce flow angle changes that result in Earth-vertical speed fluctuations without large height variations and accelerations, all well within the envelope encountered during normal research operations. Furthermore, during turns, the coordinate transformation matrix from aircraft body axis to the Earth coordinates changes rapidly allowing problems with time synchronization of the IMU, and airspeed data can readily identified.

The assumptions in the analysis are (i) the vertical component of the wind has zero mean, (ii) the horizontal wind components are steady during the turn, and

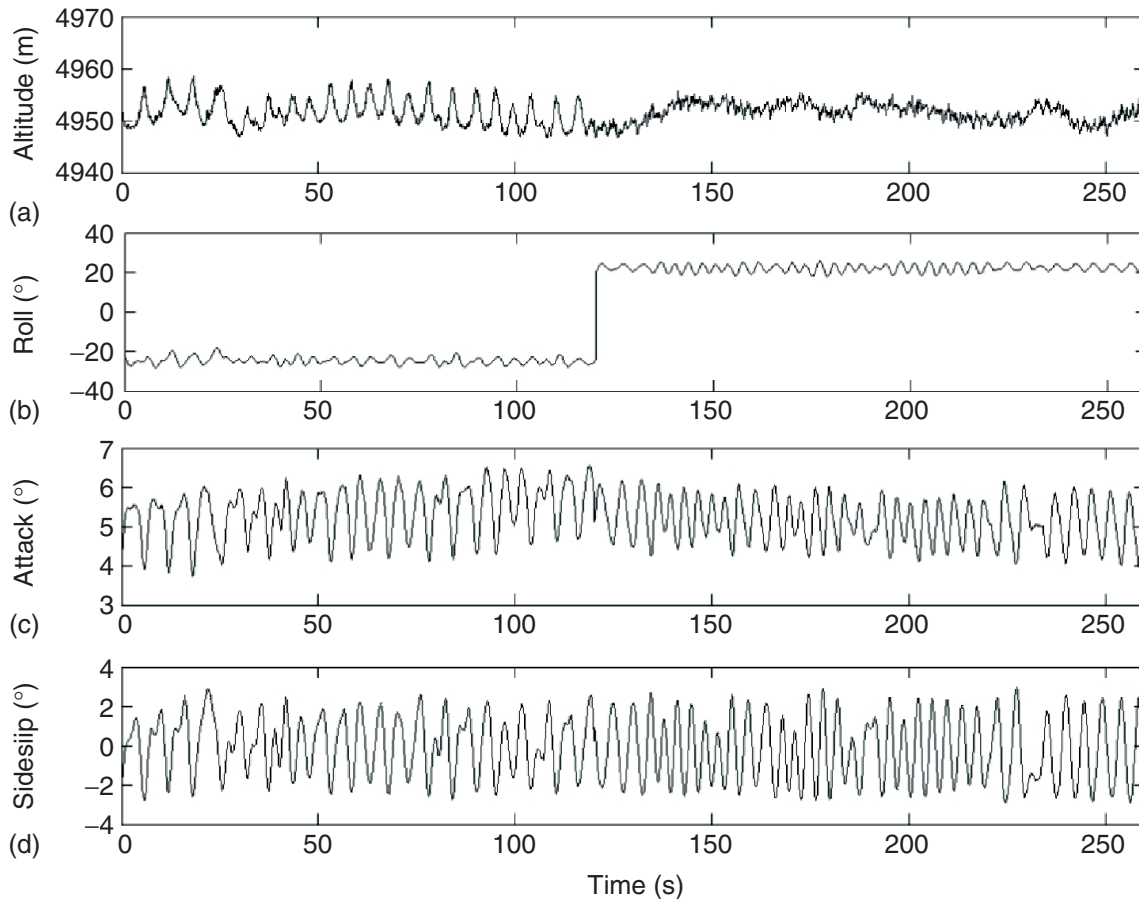


Figure A.3 Time series of 10Hz data from the University of Wyoming King Air flight on 19 March 2009. Shown are section from left turn concatenated with section from right turn. Period of induced sideslip oscillations is 10 s.

(iii) the variability of the wind components is mainly random, that is, there is no systematic spatial variability as would be caused by mountain waves, for example. The procedure finds constant coefficients and offsets that minimize a cost function expressed as $f = W^* \text{detrnd}(M)$, where W is the vertical wind component and M is the horizontal wind magnitude. The procedure results in estimates of the upwash and sidewash factors as well as the pitch, roll, and heading offsets that minimize f , evaluated using the full 3D wind equations in a nonlinear least squares solver (such as Matlab “lsqnonlin”).

The results of this calculation for the period shown in Figures A.3 and A.4 are tabulated in Table A.1. Note that the upwash factor is consistent with the value estimated from attack-pitch analysis and also from aerodynamic considerations as discussed by Crawford *et al.* (1996). Figure A.3 shows the pilot-induced inputs during the maneuver, and Figure A.4 is the resulting winds during that period after application of the coefficients and offsets. One complicating factor is that the angle offset corrections are assumed to be constant factors caused by misalignment of the inertial measurement unit with the gust probe axis, but actually, they also include time-varying inertial errors. Applying IMU/GPS corrections first would alleviate this problem.

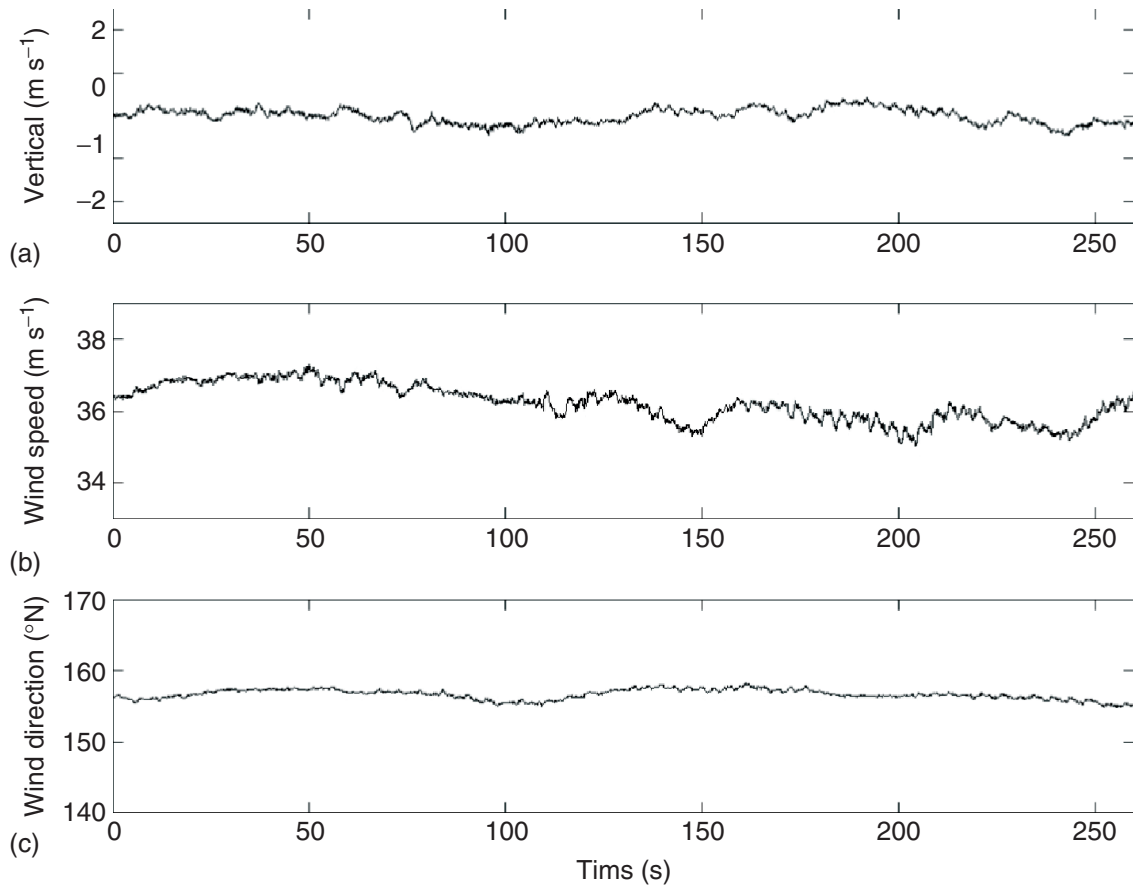


Figure A.4 Wind data after corrections from period as described in Figure 10.3.

Table A.1 Results of the least squares procedure

Upwash	Sidewash	Angle offsets [°]		
Factor	Factor	Pitch	Roll	Heading
0.759	0.776	0.290	-0.534	0.126

A.2 Small-Scale Turbulence

A.2.1 Sampling and Sensor Resolution

Time series of random variables in turbulence (e.g., for velocity components or temperature) exhibit a wide range of frequency components. A practical measurement question, therefore, is how fast should the sampling be to resolve a signal with maximum frequency f_{\max} ? The Nyquist theorem states that the sampling frequency f_s has to be at least two times of f_{\max} , i.e., $f_s \geq 2 \cdot f_{\max}$. If the signal is

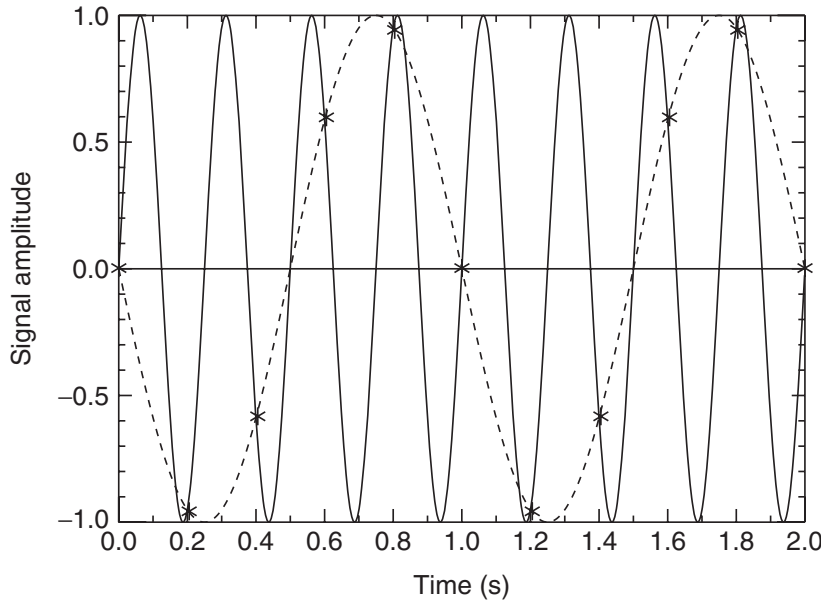


Figure A.5 The aliasing effect: a sinusoidal signal with a frequency $f = 4$ Hz is sampled with a frequency of $f_s = 5$ Hz, which violates the Nyquist theorem. The sampled points are represented as black stars and fit with a phase-shifted signal with $f = 1$ Hz.

sampled with $f_s < 2 \cdot f_{\max}$, from the sampled values of the signal, a waveform can be constructed with lower frequency. This effect is called *aliasing* and is demonstrated in Figure A.5 in which a signal (solid black line) with $f = 4$ Hz is sampled with $f_s = 5$ Hz (stars) that fits with a phase-shifted signal of 1 Hz (dashed black line); that is, in a Fourier spectrum, one would expect a peak at 1 Hz, which does not represent the frequency of the original signal.

This effect can be solved by using a sufficiently high sampling frequency (e.g., $f_s \geq 2 \cdot f_{\max}$). Since the maximum frequency of a signal is often unknown and the temporal resolution mainly depends on the sensor design, a low-pass filter with a cutoff frequency $f_{\text{cut}} < f_s/2$ should be applied, thereby removing the high-frequency contributions that cannot be sufficiently resolved by the sensor.

Another point that has to be considered is the required sensor resolution in comparison with the sampling frequency. Therefore, this section deals with a few basic considerations concerning sensor resolution at a given True Air Speed (TAS) and degree of turbulence in terms of the mean energy dissipation rate. On small scales, turbulence is often described by the statistics and correlation of velocity increments $\delta u(x, r) = u'(x) - u'(x + r)$, where $u'(x)$ are the velocity fluctuations ($u'(x) = u(x) - \langle u \rangle_x$, where $\langle \cdot \rangle_x$ denotes an average over the space parameter x). Here, we have simplified the problem to the longitudinal velocity component: x is the coordinate in-flight direction and r is a spatial lag in the same direction. The second-order statistics of the velocity increments can be described by second-order structure functions and its scaling behavior in the inertial subrange $\eta \ll r \ll L$. Turbulence at submeter scale with $r \leq 1$ m down to about $10 \cdot \eta$ can be assumed to be safely within the inertial subrange under most turbulence

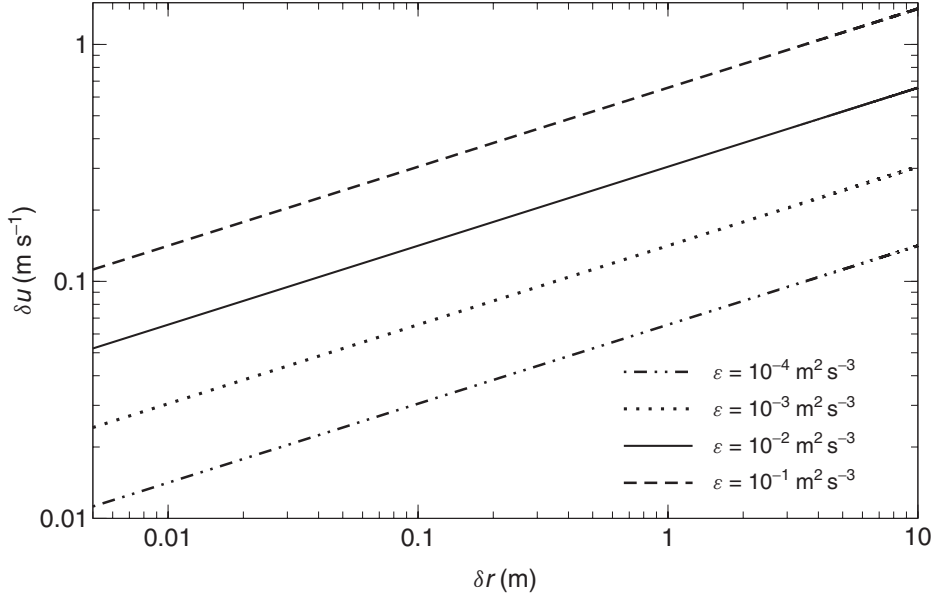


Figure A.6 Required sensor resolution δu for velocity measurements as a function of spatial resolution $\delta r = \text{TAS}/f_s$ and for different levels of turbulence described by the mean energy dissipation rate ε .

conditions and $S^{(2)}$ reads

$$S^{(2)}(r) = \left\langle (\delta u(x, r))^2 \right\rangle_x = 2(\varepsilon \cdot r)^{2/3} \quad (\text{A.14})$$

Small corrections have to be applied to the scaling exponents (2/3) to consider internal intermittency effects in high Reynolds number flows, which are negligible in this context. Note that Eq. (A.14) describes the same inertial subrange behavior as the famous $-5/3$ Kolmogorov law in the frequency domain since second-order structure functions are related to autocorrelation functions, the latter being a Fourier duality with the power spectrum.

On an aircraft, a sensor signal is usually sampled as a function of time. Time increments δt can be transformed to spatial increments δr by applying Taylor's hypothesis of "frozen turbulence": $\delta r = \text{TAS} \cdot \delta t$. This transformation can be applied if the turbulence intensity $I = u_{\text{rms}}/\text{TAS}$ is below a certain threshold, typically below $\sim 10\%$, which is fulfilled for most airborne applications due to the high TAS.

If we define the sensor resolution in such a way that the velocity increment $\delta u(r)$ in Eq. (A.14) can be resolved at given spatial resolution $\delta r \sim \text{TAS}/f_s$ and mean energy dissipation $\bar{\varepsilon}$, we can derive the following expression:

$$\delta u = \sqrt{2} \left(\bar{\varepsilon} \cdot \frac{\text{TAS}}{f_s} \right)^{1/3} \quad (\text{A.15})$$

Figure A.6 shows the required resolution δu as a function of spatial resolution δr for four different $\bar{\varepsilon}$, typical for atmospheric conditions. For example, a spatial resolution of 0.1 m at given $\text{TAS} = 100 \text{ m s}^{-1}$ requires a sample frequency of at least 1 kHz. But to resolve turbulence with a dissipation rate of $\bar{\varepsilon} = 10^{-4} \text{ m}^2 \text{ s}^{-3}$ at that same spatial scale also requires a sensor resolution of better than

$\delta u = 3 \text{ cm s}^{-1}$. It has to be considered that this estimate is based on the mean energy dissipation rate $\bar{\varepsilon}$, but atmospheric turbulence is highly variable in space and time. Locally, ε can vary a few orders of magnitude, and it is safer to estimate the sensor resolution based on a much smaller value (e.g., $\varepsilon_{\text{local}} \sim 1\%$ of $\bar{\varepsilon}$ results in a five times smaller δu).

In a similar way, the required sensor resolution for other passive scalars such as temperature or humidity can be estimated by replacing the factor “ $2 \cdot \varepsilon^{2/3}$ ” in Eq. (A.14) with the appropriate values (Warhaft, 2000).

A.3

Laser Doppler Velocimetry: Double Doppler Shift and Beats

The physical principle underlying laser Doppler velocimetry (LDV) is essentially the same as that responsible for Doppler broadening of spectral lines: the radiation source and detector can be considered stationary, with moving particles scattering light from the source to the detector. The motion of any given particle (for LDV, the particle would be an aerosol or a cloud particle) leads to a slight Doppler shift in the detected radiation. The general equation for the nonrelativistic ($v \ll c$) Doppler effect is

$$\nu' = \nu \left(\frac{c \pm v_{\text{observer}}}{c \mp v_{\text{source}}} \right) \approx \nu \left(1 \pm \frac{v_{\text{observer}}}{c} \pm \frac{v_{\text{source}}}{c} \right) \quad (\text{A.16})$$

where ν and ν' are the inherent and Doppler-shifted frequencies, respectively; c is the propagation speed; and v_{source} and v_{observer} are the velocity components of the frequency source and observer, respectively, along the source-observer path. The derivation that follows is adapted from the more detailed treatment by Davis and Schweiger (2002).

In LDV, there is a double Doppler shift because there are two “observers.” First, light emitted from a stationary source (a laser) at frequency ν is observed by a moving particle as frequency ν' . Second, light scattered by the moving particle at frequency ν' is observed by a detector (e.g., a photomultiplier tube) as frequency ν'' . The total resulting Doppler shift is therefore

$$\frac{\nu'' - \nu}{\nu} \approx \frac{v}{c} \cdot (\cos \theta_1 + \cos \theta_2) \quad (\text{A.17})$$

where v is the particle speed and again we have taken the limit $v/c \ll 1$. The angles describe the velocity components resulting from the system geometry: θ_1 is the angle between the source-particle vector and the velocity vector, and θ_2 is the angle between the particle-detector vector and the velocity vector. As should be expected, when the sum of θ_1 and θ_2 is 180° , meaning the particle lies on a straight path between the source and the detector, the double Doppler shift is zero.

The basic physical mechanism is now clear, but because the relative Doppler shift $(\nu' - \nu)/\nu \propto v/c$ we must consider how such a small Doppler shift can be measured (assuming $v \sim 10 \text{ m s}^{-1}$, we would expect relative Doppler shifts on the order of 10^{-7}). The elegant approach is to do this via heterodyne detection,

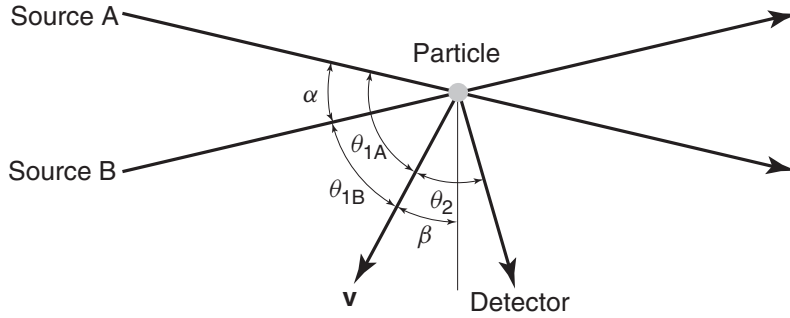


Figure A.7 Geometry of the heterodyne detection method for laser Doppler velocimetry. Two laser beams, denoted sources A and B, cross at their focal points with angle α . A particle passing through the beam-crossing region with velocity vector \mathbf{v} scatters light from both beams to the detector. Other angles are defined in the text.

in other words, mixing two coherent signals to obtain an easily measurable beat frequency. In practice, this can be accomplished by splitting the laser beam and then crossing the two beams: the different source-detector geometry results in slightly different Doppler shifts from each beam, as illustrated in Figure A.7. The beat frequency is equal to the difference of the two double-Doppler-shifted frequencies from sources A and B, $\Delta\nu'' \equiv \nu''_A - \nu''_B$. The two Doppler frequencies can be determined from Eq. (A.17), and noting that θ_2 is the same for both, we obtain $\Delta\nu'' = \nu(v/c)(\cos\theta_{1A} - \cos\theta_{1B})$. Defining angle α as the beam-crossing angle and angle β as that between the velocity vector and a vector perpendicular to the optical axis, these angles can be written as $\theta_{1A} = \pi/2 - \beta + \alpha/2$ and $\theta_{1B} = \pi/2 - \beta - \alpha/2$. Using the sine difference identity, it follows that

$$\Delta\nu'' = 2\nu \cdot \frac{v}{c} \cdot \cos(\beta) \cdot \sin\left(\frac{\alpha}{2}\right) \quad (\text{A.18})$$

This result has several interesting implications. First, the beat frequency depends on the beam-crossing angle, so this is a parameter that must be accurately determined in the instrument setup. Second, the beat frequency is independent of the detector location, perhaps a nonintuitive result that is contrary to the single-source geometry (although the signal-to-noise ratio may depend on detector location due to the angular dependence of light scattering). Third, the beat frequency is proportional to the component of the particle motion lying in the plane of the crossing beams and perpendicular to the optical axis.

A.4

Scattering and Extinction of Electromagnetic Radiation by Particles

A.4.1

Approximate Solutions of Light Scattering Problems as Used in the Processing Software of Optical Particle Spectrometers

Light scattering methods are widely used in studies of turbid media such as atmospheric aerosol and clouds. They are based on the fact that the intensity and

polarization of scattered light depends on the physical and chemical properties of the object from which light has been scattered. The advantage of light scattering methods is because they do not disturb the medium under study and enable investigations of dynamic processes in turbid media with high temporal resolution. The same applies to light extinction techniques in which the attenuation of a direct beam is studied.

The shortcomings of the light scattering and extinction techniques for particle sizing as compared, for example, to microscopy and digital imaging are due to their indirect nature. For instance, if we limit ourselves to the case of single scattering by a unit volume filled with spherical particles (e.g., as those present in water clouds and fogs), the intensity of scattered light I_{sca} at the wavelength λ in the direction specified by the scattering angle θ can be presented as

$$I_{\text{sca}}(\lambda, \theta) = B \cdot \int_{a_1}^{a_2} I(\lambda, m, a, \theta) \cdot n(a) da \quad (\text{A.19})$$

where $I(\lambda, m, a, \theta)$ is the contribution to the detected signal by a single sphere with the radius a , m is the complex refractive index of particles, and $n(a)$ is the Particle Size Distribution (PSD). It is assumed that only particles with radii between a_1 and a_2 are present in the scattering volume. The calibration constant B depends on the incident light intensity and also on a particular experimental setup. The value of $I(\lambda, m, a, \theta)$ can be presented via dimensionless Mie intensities i_1, i_2 (van de Hulst 1981) as $I(\lambda, m, a, \theta) = (i_1 + i_2)/2$. The parameter $C_{\text{sca}}(\lambda, m, a, \theta) = (i_1 + i_2)/(2k^2)$ has a dimension of the area ($k = 2\pi/\lambda$) and is called the *differential scattering cross section* (for a single particle).

Clearly, it follows

$$\int_{a_1}^{a_2} n(a) da = N \quad (\text{A.20})$$

where N is the number of particles of all sizes between a_1 and a_2 in the unit volume. The directional scattering coefficient is defined as $\beta_{\text{sca}} = N \langle C_{\text{sca}}(\theta) \rangle$, where the brackets here and below mean averaging with respect to the size distribution $f(a) = n(a)/N$, namely,

$$\langle C_{\text{sca}}(\theta) \rangle = \int_{a_1}^{a_2} C_{\text{sca}}(\lambda, m, a, \theta) \cdot f(a) da \quad (\text{A.21})$$

Therefore, we conclude that for the determination of PSD $n(a)$, one needs to solve the integral Eq. (A.19) for a given set of measured functions C_{sca} , for example, at several angles θ . As a matter of fact, this task belongs to a broad field of ill-posed problems and not always has a solution. Therefore, careful selection of the angular interval where measurements are performed is needed. In the case of large spherical particles such as fog and cloud droplets ($a \gg \lambda$ in the VIS), there are several ranges of scattering angles, where the scattered light is most sensitive

to the size of particles. They include the range of forward-scattering ($\theta \rightarrow 0$) and backscattering ($\theta \rightarrow \pi$) angles and also the scattering in the vicinity of the rainbow angle ($\theta = 138^\circ$) (van de Hulst, 1981). The Single-Particle Response Function (SPRF) $I(\lambda, m, a, \theta)$ can be presented in the first approximation as (van de Hulst, 1981)

$$I(\lambda, m, a, \theta) = \left(\frac{x}{\theta}\right)^2 \cdot J_1^2(x \cdot \theta) \quad (\text{A.22})$$

as $\theta \rightarrow 0$. Here, $J_1^2(x \cdot \theta)$ is the Bessel function and $x = 2\pi a/\lambda$ is the size parameter. The Bessel function $J_1^2(x \cdot \theta)$ is approximately equal to $x\theta/\lambda$ at small scattering angles. Therefore, we conclude that $I(\lambda, m, a, \theta) = x^4/4$ and the scattered energy is proportional to the squared geometrical cross section of the particle, as $\theta \rightarrow 0$. It follows that the angular distribution of SPRF depends on the ratio of the size of a particle to the wavelength, the distribution being more narrow for larger particles. Generally, the Bessel function $J_1^2(x\theta)$ oscillates and the first minimum is located at $x\theta_{\min} \approx 3.832$. This gives for a typical droplet with $x = 100$: $\theta_{\min} = 0.03832$ or about 2.2° . For larger droplets and crystals with the characteristic size parameter $x \sim 1000$, the value of θ_{\min} is about 0.2° . Taking into account that most of the energy is concentrated within the first ring ($\theta < \theta_{\min}$) and the fact that the influence of the direct incident light must be eliminated, the construction of the corresponding measurement system is not trivial and powerful lenses with large focal lengths must be used.

Equation (A.22) has a very limited range of applicability. For smaller spherical droplets, the Mie theory (Mie 1908) must be used. In particular, the refractive index of particles must be taken into account in calculations. In the case of large concentrations of scatterers, the small-angle multiple scattering must be accounted for. Equation (A.22) is also not valid for nonspherical particles. Let us take the example of a single ellipsoidal particle. Then clearly, the diffraction pattern is not symmetrical with respect to the incident beam. The forward-scattering pattern becomes symmetric with respect to the incident light only in the case of collections of randomly oriented particles.

In the case of a single crystal and at small scattering angles, the calculations of SPRF can be performed using the scalar Fraunhofer approximation:

$$I(u, v) = \Upsilon \cdot \left| \int \int \xi(x', y') \cdot \exp[-i \cdot k(u \cdot x' + v \cdot y')] dx' dy' \right|^2 \quad (\text{A.23})$$

Here $\Upsilon = k^2/(2\pi)$, S is the geometrical cross section of the particle in the plane perpendicular to the incident beam, $\xi(x', y')$ is the aperture factor, and $u = X/R$ and $v = Y/R$ are the angular coordinates in the observation plane located at the distance R from the particle. (X, Y) and (x', y') are coordinates in the observation and object planes, respectively. In the Fraunhofer approximation, a particle is substituted by an aperture having the same size and shape as the projection of a particle on the plane perpendicular to the incident beam direction. The aperture factor is equal to unity if it is assumed that the plane wave inside the aperture is the same as in the free space. In particular, Eq. (A.22) follows from Eq. (A.23) under

this assumption in the special case of spherical particles (van de Hulst, 1981). The generalization to account for the refractive index of particles (e.g., for small crystals) is also possible (van de Hulst, 1981). For collections of randomly oriented particles (e.g., hexagonal crystals in glaciated clouds), Eq. (A.23) must be averaged with respect to the corresponding Euler angles. Analytical calculations cannot be performed in this case and computer simulations are needed. An interesting result is that the Fraunhofer diffraction pattern of a single randomly oriented irregularly shaped particle (ISP) is equivalent to that of polydispersed spheres. The parameters of such a polydispersion depend on the parameters of ISP. The corresponding theory was developed by Shifrin *et al.* (1984).

The measurements of angular scattering $\beta(\lambda, \theta) = N \langle C_{\text{sca}} \rangle$ and extinction $\epsilon(\lambda) = N \langle C_{\text{ext}} \rangle$ (C_{ext} is the extinction cross section) coefficients of clouds are of importance not only for finding the size distributions and concentration of particles but also because these are important quantities themselves. In particular, remote sensing of clouds is based on radiative transfer modeling, where $\beta(\lambda, \theta)$ and $\epsilon(\lambda)$ are considered as an input. In addition, the total scattering coefficient

$$\sigma = 2\pi \int_0^\pi \beta(\lambda, \theta) \cdot \sin \theta d\theta \quad (\text{A.24})$$

where the phase function $p(\theta) = 4\pi \cdot \beta(\theta)/\sigma$, the single scattering albedo $\omega_0 = \sigma/\epsilon$, and the absorption coefficient $k = \epsilon - \sigma$ are used. The phase function is normalized as follows:

$$\frac{1}{2} = \int_0^\pi p(\theta) \cdot \sin \theta d\theta \quad (\text{A.25})$$

In radiative transfer studies, the asymmetry parameter

$$g = \frac{1}{2} \int_0^\pi p(\theta) \sin \theta \cdot \cos \theta d\theta \quad (\text{A.26})$$

is often used as well. The values of g depend on the size and shape of particles, and they are often close to 0.75 for ice clouds and 0.85 for water clouds. This means that ice clouds generally are more reflective (in the VIS, where $k \approx 0$) as compared to water clouds of the same optical thickness:

$$\tau = \int_{l_1}^{l_2} \epsilon(z) dz \quad (\text{A.27})$$

where z is the vertical coordinate and l_1 and l_2 are the corresponding cloud boundaries.

It can be shown using both the Mie theory and the geometrical optics calculations that in the case of nonabsorbing large ($a \gg \lambda$) particles, which exist in tropospheric clouds, it follows

$$\sigma = 2N \cdot \langle S \rangle \quad (\text{A.28})$$

where S is the geometrical cross section of particles ($S = \pi \cdot a^2$ for spheres). The angular integration of the geometrical optics part of scattering field, as shown in Eq. (A.24), is somewhat involved. However, the diffraction part can be easily integrated resulting in

$$\begin{aligned} C_{\text{sca}}^{\text{d}}(\lambda, m, a) &= 2\pi \cdot k^{-2} \int_0^{\pi} \left(\frac{x}{\theta}\right)^2 \cdot J_1^2(x\theta) \cdot \sin \theta d\theta \\ &\approx 2\pi \cdot a^2 \int_0^{\infty} J_1^2(\gamma) \cdot \gamma^{-1} d\gamma \\ &= \pi \cdot a^2 \end{aligned} \quad (\text{A.29})$$

in the case of a single sphere with the radius a as it should be. Here, we accounted for the property of the Bessel functions (the orthogonality relation):

$$2 \int_0^{\infty} J_1^2(\gamma) \cdot \gamma^{-1} d\gamma = 1 \quad (\text{A.30})$$

The geometrical optics part of the scattering cross section is equal to πa^2 as well (for nonabsorbing particles).

The analytical integration can be performed up to any scattering angle in the forward-scattering region and not for the whole diffraction peak as in Eq. (A.29):

$$\begin{aligned} C_{\text{sca}}^{\text{d}}(\lambda, m, a, \theta_0) &\approx 2\pi \cdot a^2 \int_0^{ka\theta_0} J_1^2(\gamma) \cdot \gamma^{-1} d\gamma \\ &= \pi \cdot a^2 \cdot [1 - J_0^2(k \cdot a \cdot \theta_0) - J_1^2(k \cdot a \cdot \theta_0)] \end{aligned} \quad (\text{A.31})$$

In the calculation of this integral, we used the property

$$\frac{J_1^2(\gamma)}{\gamma} = J_0(\gamma) \cdot J_1(\gamma) - J_1(\gamma) \cdot J_1'(\gamma) \quad (\text{A.32})$$

and the corresponding values of tabular integrals. Here, J_1' is the derivative of the Bessel function. Therefore, it follows that the fraction of scattered energy ΔC_{sca} in the angular range $\epsilon \in [\theta_1, \theta_2]$ is proportional to the following function:

$$\Delta C_{\text{sca}} = \pi \cdot a^2 \cdot [J_0^2(k \cdot a \cdot \theta_1) + J_1^2(k \cdot a \cdot \theta_1) - J_0^2(k \cdot a \cdot \theta_2) - J_1^2(k \cdot a \cdot \theta_2)] \quad (\text{A.33})$$

This equation (averaged with respect to the PSD) is the basis for the measurements of PSDs in a number of devices.

Not only scattering but also light extinction can be used to determine the size distribution of particles. The extinction coefficient can be written as

$$\epsilon = N \int_0^{\infty} C_{\text{ext}}(a) \cdot f(a) da \quad (\text{A.34})$$

Usually, the spectral measurements of ϵ are used in the optics of turbid media to determine $f(a)$ solving Eq. (A.34). The value of C_{ext} is close to $2S$ for large particles (at the VIS wavelengths). It follows

$$\epsilon_{\text{vis}} = 2N \cdot \langle S \rangle = 2\pi \cdot N \cdot \langle a^2 \rangle \quad (\text{A.35})$$

or $\epsilon_{\text{vis}} = 1.5 \text{LWC}/a_{\text{ef}}\rho$, where $\text{LWC} = N \cdot \rho \cdot \langle V \rangle$, ρ is the density of water, $\langle V \rangle$ is the average volume of particles, and $a_{\text{ef}} = 3 \langle V \rangle / (4 \langle S \rangle)$ is the effective radius of particles. The dimensionless volume concentration $C_v = N \langle V \rangle$ is also often used in various theoretical calculations.

The measured extinction coefficient gives the total surface area of particles in unit volume $\Sigma = 4\pi N \langle a^2 \rangle$, namely, $\Sigma = 2\epsilon$. The information on PSD is then lost. For thermal IR wavelengths (e.g., 12 μm), particles are highly absorbing and small as compared to the wavelength. Then one derives (van de Hulst, 1981) for the sphere of the volume V :

$$C_{\text{ext}} = \frac{9\alpha \cdot n \cdot V}{|m^2 + 2|^2} \quad (\text{A.36})$$

$$\epsilon_{\text{TIR}} = \zeta \cdot N \cdot \langle V \rangle \quad (\text{A.37})$$

where

$$\zeta = \frac{9\alpha \cdot n}{|m^2 + 2|^2} \quad \alpha = \frac{4\pi \cdot \chi}{\lambda} \quad (\text{A.38})$$

$m = n - i \cdot \chi$ is the complex refractive index of the particles. It follows from Eqs. (A.34) and (A.36) that the liquid water content can be obtained directly from ϵ_{TIR} , namely, one derives

$$\text{LWC} = \frac{\epsilon_{\text{TIR}} \cdot \rho}{\zeta} \quad (\text{A.39})$$

Also, the effective radius of particles can be determined (Eqs. A.35–A.37):

$$a_{\text{ef}} = \frac{3\epsilon_{\text{TIR}}}{2\zeta \cdot \epsilon_{\text{vis}}} \quad (\text{A.40})$$

The application of these theoretical results in various optical instruments is given in Chapter 5.

A.4.2

Light Scattering Theory for Specific Spectrometers

The operating principle of the FSSP, CDP, CAS, CAS-DPOL, CPSD, and SID is based on the concept of light scattering described earlier, that is, the intensity of scattered light depends on the particle size and can be predicted theoretically if the shape and refractive index of a particle is known, as well as the wavelength of the incident light, as described in detail in Section A.4.1. The important point is that the intensity of light scattered by a particle varies with the angle with respect to the incident light. If the particle is spherical and of homogeneous composition, the scattered intensity is symmetric around the axis parallel with

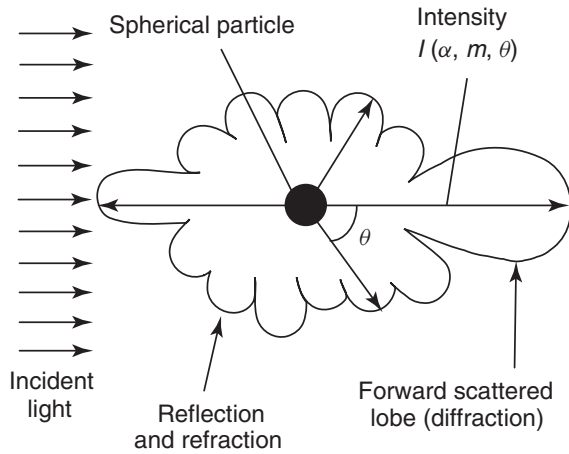


Figure A.8 The intensity of scattered light as a function of angle with respect to the incident ray for a typical spherical particle.

the incident wave but varies in intensity from 0° to 180° , where 0° is the most forward scattering and 180° is directly backward. Figure A.8 shows an example of the angular pattern of scattering. This angular dependency of the scattering around a spherical particle can be calculated using the equations that were developed by Mie (1908) for a specific diameter, refractive index, and incident wavelength.

This theory is applied in optical particle counters (OPCs) by collecting scattered light from particles that pass through a light beam of controlled intensity and wavelength and by converting the photons to an electrical signal whose amplitude can be subsequently related back to the size of the particle.

The property of a particle to interact with light is usually described by its scattering cross section, σ_s . This is the product of the scattering efficiency, θ_s , and cross-sectional area, $\pi/4 \cdot D^2$, where D is the particle diameter. If we have an optical system that collects light over a range of angles and we measure the intensity of scattered light collected from a particle, we can then determine the particle size from the calculated scattering cross sections by integrating over the range of angles used in the instrument. The single-particle light scattering spectrometers differ mostly in the collection angles that are used in each system.

A.4.3

Imaging Theory

Section 5.3.4 described the optical array probes (OAPs) that capture images of cloud particles using optical imaging. Here, the theory underlying the measurement is described in more detail.

Consider a plane wave that is incident, perpendicular to an opaque screen (Figure A.8). Following Babinet's principle, the amplitude of the diffracted wave at

point Q can be presented as (Born and Wolf, 2003)

$$U(Q) = U_a(Q) + U_b(Q) \quad (\text{A.41})$$

where $U_a(Q)$ is the amplitude of the diffracted wave, if the opaque screen is in place, and $U_b(Q)$ is the diffracted wave when the aperture, with the same shape as the screen, is in place. In the frame of the Fresnel–Kirchhoff diffraction theory, $U_a(Q)$ and $U_b(Q)$ can be written as (Baker and Copson, 1950)

$$U_a(Q) = \begin{cases} \exp(i \cdot K \vec{k} \cdot \vec{g}) & \text{if point } Q \text{ is outside the geometrical shadow} \\ 0 & \text{if point } Q \text{ is inside the geometrical shadow} \end{cases} \quad (\text{A.42})$$

$$U_b = -\frac{1}{4\pi} \oint_{\Gamma} \exp(i \cdot K \vec{k} \cdot \vec{g}) \cdot \frac{\exp(iKS)(\vec{s} \times \vec{k})}{S \cdot (1 + \vec{k} \cdot \vec{s})} d\vec{l} \quad (\text{A.43})$$

where $\vec{k} = \vec{K}/|\vec{K}|$ is a unit vector in the direction of the wave propagation, $K = 2\pi/\lambda$ is the wave number, \vec{p} is the radius vector of point P on the contour Γ , S is the differential element along the contour Γ , S is the distance between points P and Q, and \vec{s} is the unit vector in the PQ direction.

Integration of $U_b(Q)$ in Eq. (A.43) is carried along the contour of the boundary of the geometrical shadow. Eqs. (A.41)–(A.43) give a general description of the Fresnel diffraction by an opaque screen with an arbitrary shape. For the case of an opaque disk, Eqs. (A.42) and (A.43) can be transformed into (Korolev *et al.* 1991)

$$U_a(Q) = \begin{cases} \exp(i \cdot k \cdot Z) & \text{if } r > R \\ 0 & \text{if } r \leq R \end{cases} \quad (\text{A.44})$$

$$U_b(Q) = -\frac{1}{4\pi} \int_0^{2\pi} \frac{\exp(i \cdot k \cdot S) \cdot (R^2 - R \cdot r \cdot \cos \alpha)}{S \cdot (S - Z)} d\alpha \quad (\text{A.45})$$

where R is the radius of the opaque disk, r is the distance from the center of the image to the point Q , $k = 2/\lambda$ is the wavenumber, Z is the distance between the disk and its image, and S can be found as $S = (Z^2 + R^2 + r^2 - 3R \cdot r \cdot \cos \alpha)^{\frac{1}{2}}$.

The intensity of the light at point Q (Figure A.9) is calculated as

$$I(Q) = |U_a(Q) + U_b(Q)|^2 \quad (\text{A.46})$$

The analysis of Eqs. (A.44)–(A.46) yields the following properties of diffraction images by an opaque disk (Korolev *et al.*, 1991):

- 1) The diffraction image can be presented as a function of only one dimensionless variable:

$$Z_d = \frac{\lambda \cdot |Z|}{R^2} \quad (\text{A.47})$$

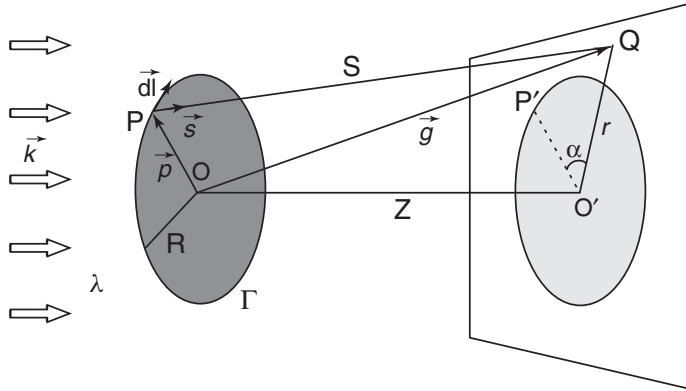


Figure A.9 A schematic explaining calculation of diffraction by an opaque disk.

- 2) Two droplets with different diameters give the same diffraction image if $|Z_1|/|Z_2| = R_1^2/R_2^2$. The images for such droplets are different only by the scale factor R_1/R_2 .
- 3) The diffraction image does not depend on the sign of Z . The diffraction image of the same droplet will be the same at equal distances on opposite sides of the object plane.

A.4.4

Holography Theory

For a clear understanding of the holographic method, an analytical model can be considered for a hologram resulting from a single water droplet. Holograms recorded in a liquid cloud typically involve the interference of a reference beam and a wave scattered by transparent, on the order of 10–100 μm diameter, spherical water droplets. This would suggest a complete solution using the Mie theory to describe the electric field due to scattering from a sphere and its interference with the incident plane wave. However, we note that the particle size and scattering geometry allow for several useful approximations.

Because size parameters are large ($\pi \cdot d/\lambda > 60$) and in-line holographic systems observe only forward-scattered light (scattering angle $< 10^\circ$), to a good approximation, we may neglect the complexities of the Mie theory and treat the scattered wave as diffraction from an opaque disk with the same diameter as the water droplet (Bohren and Huffman 1983). Furthermore, in the droplet size range considered, most holographic systems operate in the far field ($z \gg d^2/\lambda \sim 2\text{--}20\text{ mm}$), so we may treat the scattered wave with the Fraunhofer approximation. In practice, digital reconstruction of the holograms is normally carried out using more general approaches because actual conditions do not always satisfy the far-field constraint (for example, ice particles larger than 100 μm in extent).

To develop the analytical model, we consider an opaque disk of diameter d located at $z = 0$ and centered on the optical axis, where the z -coordinate is taken to be the optical axis. We use (x, y) as coordinates in the (far-field) diffraction plane,

also perpendicular to the optical axis. Making the foregoing assumptions (far-field, large size parameter, etc.), an analytical expression for the total electric field E_H can be obtained. Defining $r = (x^2 + y^2)^{1/2}$, $C = \pi \cdot d^2 / (4\lambda \cdot z)$, $Q(r) = 2J_1(\xi) / \xi$ with $\xi = \pi r \cdot d / (\lambda \cdot z)$, and J_1 is the first order Bessel function of the first kind, $\Phi(r) = \pi r^2 / (\lambda \cdot z)$, the resultant field E_H and measured intensity $I_H(r) = E_H(r) \cdot E_H^*(r)$ take the form

$$E_H = 1 - C \cdot Q \cdot i^{-1} \cdot \exp(i\Phi) \quad (\text{A.48})$$

$$I_H = 1 - 2C \cdot Q \cdot \sin(\Phi) + C^2 \cdot Q^2 \quad (\text{A.49})$$

The first term in Eq. (A.49) is the background intensity and $(C \cdot Q)^2$ is the negligible scattered intensity (diffraction) term. The middle term produces a modulated fringe pattern that depends on both particle size and z -position. In the Fraunhofer limit, therefore, the hologram obtained from a population of cloud droplets may be approximated as the superposition of the fields, one for each particle, with z and d adjusted appropriately for droplet position and size, respectively. In practice, the cloud of particles is sufficiently dilute that the interference of the waves from various particles can be neglected.

Equation (A.49) demonstrates several important features of holography. First, the interference term $\Phi(r)$ depends only on the position of the particle along the optical axis, not on its diameter d . Hence, the spatial frequencies in this term alone contain sufficient information to provide the particle's position along the optical axis (the position in the (x, y) plane is easily determined). Also, the spatial frequency increases radially as $r = z$, so that the desired depth of field of the instrument places a constraint on the spatial resolution of the detector. Note also that the increasing spatial frequency with r suggests that the finite pixel size limits the maximum sharpness attainable in reconstructed images. Both of these conclusions can be obtained by considering in-line holography for a point particle, but the disk aperture model makes it clear that the interference fringe pattern described by the $\sin[\Phi(r)]$ term contains information on particle position, while the modulation of this pattern by the term $2C \cdot Q(r)$, depends on both z and d , as expected from common experience with diffraction by a circular aperture.

A.5 LIDAR and RADAR Observations

A.5.1 Overview of Airborne RADAR Systems

Table A.2 on the following pages provides an overview of the characteristics of airborne RADAR systems designed for observations of clouds and precipitation. This material complements and extends what is given in Section 9.3.4.

Entries in the table are arranged in chronological order, column by column, using the date on which a particular unit was first placed in service. This ordering incorporates the combined influences of the evolution of scientific needs and of the technology of airborne RADAR systems over nearly four decades and allows readers to place in perspective the development of these observational tools and the results obtained with them.

Each column lists the main technical specifications of the RADAR, the aircraft on which it was deployed, and the principal objectives that governed the design of the RADAR. In the last row, links are given to web pages where more detailed information is available about the RADAR unit and about the scientific results obtained using data from it. Those pages usually also contain links for contacting the principal investigators in charge of the science teams associated with the RADAR. The data in the table were supplied by those investigators.

A.5.2

Results of Airborne RADAR Observations – Some Examples

Examples are presented on the following pages of the variety of observations possible with airborne RADAR systems. Figures A.10–10.18 demonstrate the possibilities, and also the limitations, of what can be learned with the use of the airborne RADARs currently in use. The cases selected here demonstrate the use of different RADAR systems and platforms, applications in various projects, and the interpretations of observations making use of numerous RADAR parameters. Brief explanations of each case are presented in the figure captions.

Readers might find it useful to refer to Table for the specifications of the RADARs used to generate the data used in the examples. The principles of operation and the factors that determine the nature of airborne RADAR observations are detailed in Section 9.5.

A.6

Processing Toolbox

Within the EUFAR framework, the Standards and Protocols (N6SP) group is tasked with developing recommendations for common solutions in data formats and metadata and data processing. Establishment of standards in these areas will reduce errors in data usage and provide a common platform for comparison, exchange, and dissemination of data. In addition, these developments can provide a useful resource for both new and experienced users of airborne science data. More information on these developments can be found on the N6SP wiki, hosted at <http://www.eufar.net/N6SP>.

As a part of the N6SP common solutions, a software toolbox has been developed to provide a common platform for processing airborne measurements. This toolbox, known as the *EUFAR General Airborne Data-Processing Software*

Table A.2 Overview of airborne RADARs operate in the K- or W-band, with X-band used less frequently.

DESIGNATION:	NOAA P-3 Lower Fuselage Radar	NOAA P-3 Parabolic Antenna	NOAA P-3 French dual Flat plate	ELDORA
Full name of radar	Lower Fuselage Radar	Tail Doppler radar	Tail Doppler radar	Electra Doppler Radar
Aircraft(s) carrying the unit	NOAA WP-3D both N42RF and N43RF	NOAA WP-3D either N42RF or N43RF	NOAA WP-3D either N42RF or N43RF	NRL P3
Main purpose	precipitation, particularly in hurricanes but also in other weather such as severe storms	winds and precipitation, particularly in hurricanes but also in other weather such as severe storms	winds and precipitation, particularly in hurricanes but also in other weather such as severe storms	3D kinematic structures of precipitation systems and clear air boundary layer
Antenna configuration	parabolic antenna that rotates in a plane parallel to the ground, while being steerable up to 5 degrees up or down of plane parallel to the ground	parabolic antenna that rotates completely around the axis of the fuselage, while being steerable up to 25 degrees fore and aft of the plane normal to the fuselage	French-built dual flat-plane antennas that rotate completely around the axis along the fuselage, with beams 20 degrees fore or aft of a plane normal to the fuselage	dual-flat plate, slotted waveguide antenna, conical scan, dual-beam (15-19 deg FORE and AFT)
Year placed in service	1976	1976	1991	Jan 1993
Operating frequency (GHz)	5.37 (C-band)	9.315±0.0116 (X-band)	9.315±0.0116 (X-band)	9.3-9.8 (X-band)
Peak power (kW)	70	60	60	35-40
Usable signal level (best configuration)	0 dBZ	-10 dBZ at 10 km	-10 at 10 km	-12 dBZ at 10 km
Calibration accuracy (dBZ)	2	2	2	1.5
Best range resolution (m)	250	75	75	37.5
Beam width (degrees)	4.1 (vertical), 1.1 (horizontal)	1.35 perpendicular to scan direction, 1.90 along scan direction	2	1.8
Doppler capability yes/no	no	yes	yes	Yes
Polarization diversity yes/no	no	no	no	No
Special features				frequency diversity
Link to detailed information	http://www.aoml.noaa.gov/hrd/HRD-P3_radar.html	http://www.aoml.noaa.gov/hrd/HRD-P3_radar.html	http://www.aoml.noaa.gov/hrd/HRD-P3_radar.html	http://www.eol.ucar.edu/instrumentation/airborne-instruments/eldora/eldora

DESIGNATION:	EDOP	WCR	SPIDER	EC CPR	RASTA
Full name of radar	ER-2 Doppler Radar	Wyoming Cloud Radar	Super Polarimetric Ice-crystal Detection and Explication Radar	Environment Canada Cloud Profiling Radar	Radar System Airborne
Aircraft(s) carrying the unit	NASA ER-2	University of Wyoming King Air 200T or NSF/NCAR C-130	Gulfstream II (operated by Diamond Air Service Co. Ltd.)	NRC Convair-580	Falcon 20, ATR-42
Main purpose	vertical structure of deep precipitation systems, hurricanes, and thunderstorms from high-altitude nadir viewing	atmospheric research: clouds, light precipitation	cloud microphysics	cloud microphysics	cloud microphysics and dynamics, light precipitation
Antenna configuration	two fixed beams: nadir and 35 deg forward looking	up to 5 single-polarization antennas, currently using 1 dual-pol and 3 single-pol antennas on the King Air and 3 single-pol antennas on the C-130	offset Gregorian type antenna, -40 to +95 degree scan across flight direction	Fixed zenith and nadir-looking single pol 30.5 cm antennas	Falcon 20 : 3 beams downward (45 cm antennas: nadir,), 2 beams upward. ATR42 : 2 beams downward
Year placed in service	Sept 1993	June 1995; Oct 2009	1998	1999	November 2000
Operating frequency (GHz)	9.6 (X-band)	94.92 (W-band)	95.04 (W-band)	35 (Ka-band)	95.04 (W-band)
Peak power (kW)	25 (split between two ports)	1.8 kW, 1% duty cycle	1.6	50 kW - split to 2 ports	1.8
Usable signal level (best configuration)	-20 dBZ at 10 km	-40 dBZ at 1 km	-30 dBZ at 5 km	-33 at 1 km	-35 dBZ at 1 km
Calibration accuracy (dBZ)	1	better than 2.5 dB (est.)	1		1
Best range resolution (m)	37.5	15 m	41.25	37.5	30
Beam width (degrees)	3	0.8 (max.)	0.6	2	0.5
Doppler capability yes/no	yes	yes	yes	No	yes
Polarization diversity yes/no	yes – received LDR	yes, linear, up to 2 antennas	yes	No	no
Special features		pulse pair and full Doppler spectra acquisition modes: King Air also provides an external reflector for redirecting the side-pointing beam to upward-pointing for a total of 5 fixed-beam directions			pulse pair and FFT acquisition modes (2048 pts) - reflector will be implemented in 2010 to scan a +15 degrees sector perpendicular to the aircraft heading
Link to detailed information	http://haer.gsfc.nasa.gov	http://atmos.uwyo.edu/wcr/			

Table A.2 (continued)

DESIGNATION:	APR-2	NOAA IWRAP	CRS	NAWX	HIWRAP
Full name of radar	Airborne Precipitation Radar 2nd Generation	Imaging Wind and Rain Profiler	Cloud Radar System	NRC Airborne W- and X-band Polarimetric Doppler Radar	High-altitude Imaging Rain and Wind Profiler
Aircraft(s) carrying the unit	NASA DC-8 & P-3	NOAA WP-3D either N42RF or N43RF	NASA ER-2	NRC Convair 580	NASA WB-57, Global Hawk
Main purpose	cloud and precipitation	winds and precipitation, particularly in hurricanes but also in other weather	vertical structure of clouds from high-altitude nadir viewing	atmospheric research	3D winds and reflectivity from precipitation and clouds, ocean surface winds
Antenna configuration	Dual-frequency horn, fixed collimating antenna and scanning flat plane to achieve +/- 25° scan angle in the cross-track plane	conical scan about nadir, quad-beam (30, 35, 40 and 50 deg), dual-frequency	nadir	66 cm parabolic to side; 45 cm flat plate slotted waveguide for up and down	30 cm fixed to side and down, third beam to zenith or up to 40° from vertical or side via reflector plate
Year placed in service	2001	2002	July 2002	May 2006	Jan 2010
Operating frequency (GHz)	13.4 GHz (Ku), 35.6 GHz (Ka)	5.01-5.4 (C-band), 12.87-13.92 (Ku-band)	94.155 (W-band)	9.41 (X-band)	94.05 (W-band)
Peak power (kW)	0.2 (Ku), 0.1 (Ka)	15.8	1.7	25 split between two ports	1.9
Usable signal level (best configuration)	10 dBZ (Ku), 0 dBZ (Ka) at 10 km	0 dBZ at 1 km	-28 dBZ at 10 km	-20 dBZ at 1 km	-30 dBZ at 1 km
Calibration accuracy (dBZ)	1.5	1	2	2	2
Best range resolution (m)	30	15	37.5	45	15
Beam width (degrees)	4	5-10 depending on frequency and incidence angle	0.6 x 0.8 (cross-track x along-track)	3.5 side / 5.5 nadir & zenith	0.7
Doppler capability yes/no	yes	yes	yes	yes	yes
Polarization diversity yes/no	single pol TX, dual pol Rx (for LDR)	yes, linear HH, VV (C and Ku)	yes - receive LDR	yes - linear	yes - linear
Special features	pulse compression, cross-track scanning	pulse compression, frequency diversity	four identical receiver channels connected to four antenna ports; simultaneous transmit and receive Z, ZDR, Kdp	FM Chirp Mode option. Least Mean Squared (LMS) filters provide better than -30 dB range side lobe suppression	unpressurized low-power solid state power amplifier based transceivers; pulse compression; frequency diversity
Link to detailed information	"Development of an advanced airborne precipitation radar" by Sadowy et al., Microwave Journal, (2003)	http://mirsl.ecs.umass.edu/index.pl?id=2469	http://har.gsfc.nasa.gov	http://www.nawx.nrc.gc.ca/	http://har.gsfc.nasa.gov

DESIGNATION:	G-IV Tail Doppler Radar	HCR	ACR	EXRad
Full name of radar	G-IV Tail Doppler radar	HIAPER Cloud Radar	Airborne Cloud Radar	ER-2 X-band Radar
Aircraft(s) carrying the unit	NOAA G-IV SP aircraft	NSF/NCAR G-V	NASA P-3	NASA ER-2
Main purpose	winds and precipitation, particularly in hurricanes but also in other weather	cloud microphysics	cloud and precipitation	3D winds and reflectivity from precipitation and clouds; ocean surface winds
Antenna configuration	dual-flat-plane antennas that rotate completely around the axis along the fuselage, with beams that point either a fixed 20 degrees fore or aft of the plane normal to the fuselage	lens coupled to rotating reflector positions beam anywhere between zenith and nadir	W-band lens antenna	dual-beam: conical or cross-track scan about nadir; fixed nadir
Year placed in service	2010	single-pol Jan. 2011, dual-pol July 2013	??	2010
Operating frequency (GHz)	9.3 (X-band)	94.04625 (W-band)	94.9 GHz	9.6
Peak power (kW)	7	2	1.4	9 kW, 2% duty cycle
Usable signal level (best configuration)	-12 dBZ at 10 km	-22 dBZ at 10 km	N/A	-15 dBZ at 10 km
Calibration accuracy (dBZ)	2	2	N/A	1
Best range resolution (m)	50	30	30	37.5
Beam width (degrees)	2.7	0.7	0.8	3
Doppler capability yes/no	yes	yes	yes	yes
Polarization diversity yes/no	no	yes - alternating H, V	yes	yes
Special features	pulse compression		frequency diversity	
Link to detailed information	http://www.aoml.noaa.gov/hrd/tcdir/index.htm	http://www.eol.ucar.edu/development/current-development/hcr/hiaper-cloud-radar/?searchterm=hcr	"The NASA DC-8 Airborne Cloud Radar: Design and Preliminary Results" by Sadowy et al., IGARSS Proc. (1997)	http://harr.gsfc.nasa.gov/

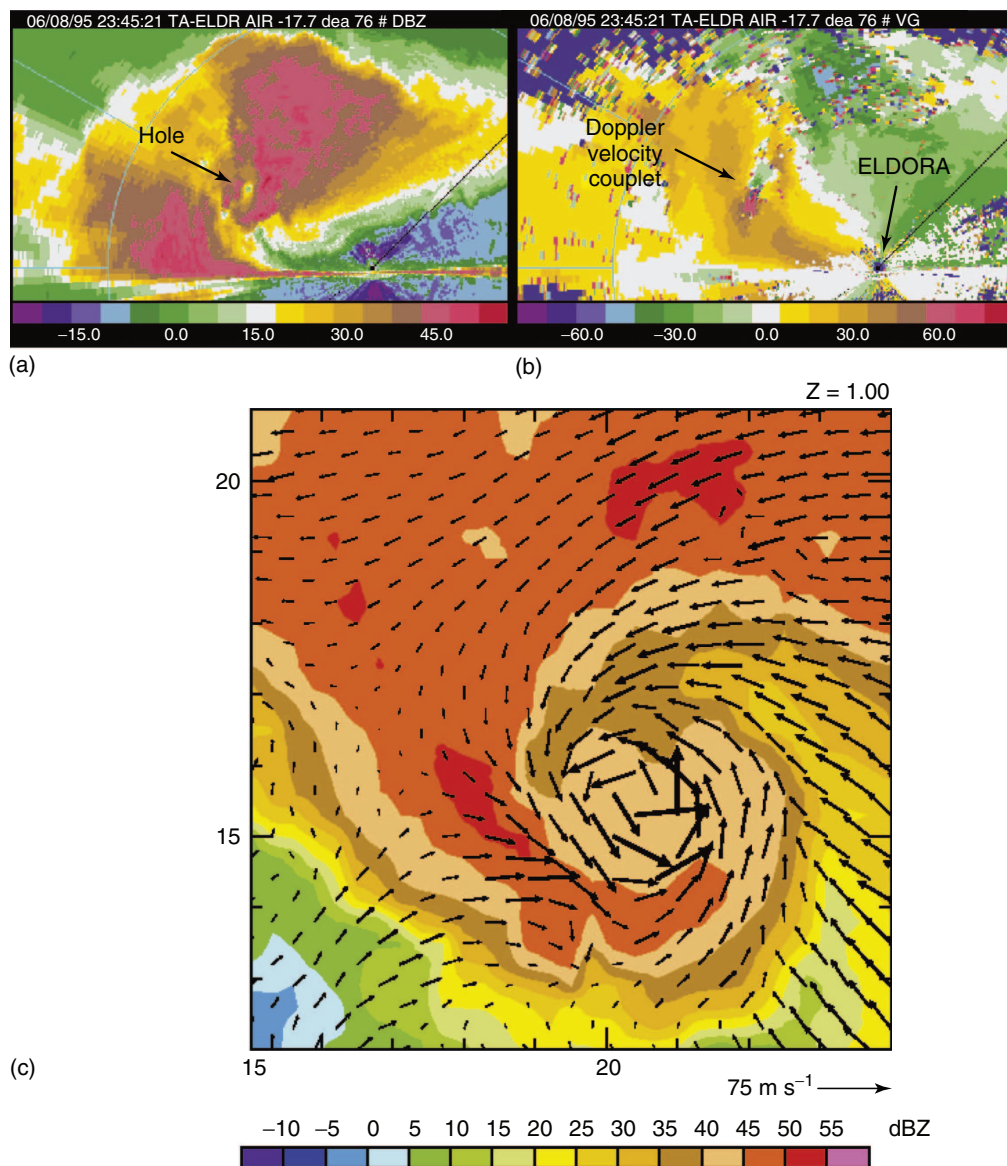


Figure A.10 The NCAR/NSF Electra with ELDORA flew by an F5 tornado near Kellerville, TX, on 8 June 1995. ELDORA's conical helix sliced through the vertically tilted tornado. Reflectivity and radial velocity are shown in (a) and (b), respectively. Precipitation particles were centrifuged out by the tornado circulation to form a weak reflectivity "hole" (a). This was associated with an intense Doppler velocity couplet (b) with $a > 30 \text{ m s}^{-1}$ approaching wind (green) and $> 80 \text{ m s}^{-1}$ receding wind (red) separated by $\sim 1 \text{ km}$. The anticyclonic rotation on this ELDORA scan inferred by the Doppler velocity couplet suggested that

the tornado vortex was vertically tilted into the page with height. The speckles in the Doppler velocity display suggested highly turbulent winds within this supercell. Horizontal wind vectors and the reflectivity of the tornado are shown in (c). The parent mesocyclone of the tornado associated with a "hook" RADAR reflectivity signature is clearly shown. With the 300 m resolution of the ELDORA data, the actual tornado circulation on the scale of 500 m could not be resolved. *Source:* Courtesy of Wen-Chao Lee. A full-resolution version of the image is at http://?/A10_eldora.pdf

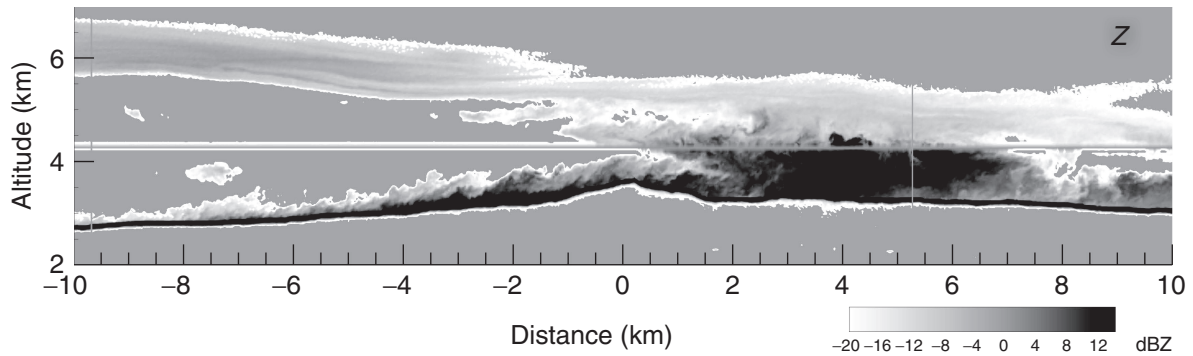


Figure A.11 Vertical section through a winter storm over the Medicine Bow Mountains of SE Wyoming (27 January 2006, 22:02 UTC). The image consists of data collected by the 95 GHz WCR (Table 10.2) onboard the Wyoming King Air as it flew at 4285 m altitude from west to east (left to right in the figure). Two antennas were used simultaneously, one pointing upward and one downward. The figure is very close to a 1 : 1 true proportion of the storm. The reflectivity scale is in dBZ. The image reveals an unexpected layer of shallow clouds right over the surface on the upwind side of the mountain range.

The near-surface echo is very likely due to blowing snow. Because of its shallow depth and low reflectivity, it would have been very difficult to detect with ground-based RADARs. On the downwind side of the ridge, a deep cloud mass is seen as the result of the merging of wave clouds (5–6 km altitude) with a cell forming there and with the snow layer near the surface. Essentially, all the echo is due to ice crystals. Temperature at flight level was -15.5°C , and ice particle concentrations reached 80l^{-1} . *Source:* Courtesy of G. Vali. To see a full-resolution image go to http://.../A11_nasa06.pdf

(EGADS), compiles processing algorithms provided by the EUFAR Expert Working Groups into a Python framework. These algorithms, many of which are based on concepts found in this book, are considered as the best practice by the community and thus can be used as a reference for future work. Integration of the algorithms is an ongoing process – there are around 20 implemented algorithms at the time of this writing, and many more will be added in the near future.

Alongside the algorithms implemented in the EGADS framework are file input and output routines for common airborne data formats (NetCDF, NASA Ames, CSV, etc.). Included in these file access routines are methods to automatically process any available metadata when reading file data. These allow EGADS to be used with most existing airborne data while following established data and metadata conventions. The EGADS package is completely free and open-source and thus can be modified as needed if other file access methods are desired.

A.6.1

Installation and Use

The EGADS is hosted for free download on Google Code at <http://eufar-egads.googlecode.com> or through the Python Package Index (PyPI). The EGADS is a

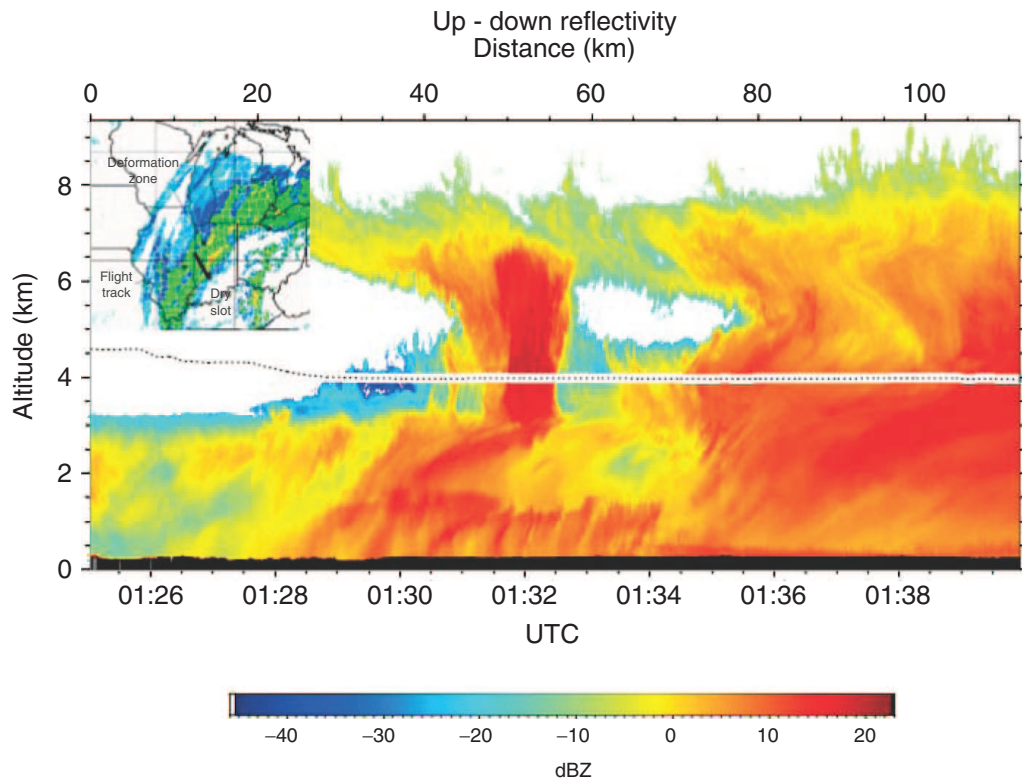


Figure A.12 Wyoming Cloud RADAR reflectivity image, which was taken as the NCAR C-130 passed from the dry slot to the deformation zone north of the center of a continental cyclone, illustrates the triggering of convection along the dry slot–cloud interface. The data were collected during

the US NSF funded “Profiling of Winter Storms,” or PLOWS, experiment over the states of Illinois and Indiana on 2 December 2009. *Source:* Courtesy of Samuel Haimov and Bob Rauber. To see a full-resolution image go to [http:// ... / A12_plows.pdf](http://.../A12_plows.pdf)

Python-based library; thus, to use it, Python version 2.5 or higher must be installed on your system. The toolbox depends on several commonly available libraries, which are all also freely available. A list of these libraries can be found in the included EGADS documentation. To install EGADS, simply download the code from Google Code and follow the included instructions, or install through Python’s easy_install feature (see documentation included with EGADS for more detailed installation instructions for either method).

To use EGADS, import the package from the Python command line, and any of the included routines can then be used. The following script is a short example of the EGADS being used to process a series of data files.

```
#!/usr/bin/env python

# import egads package
import egads
```

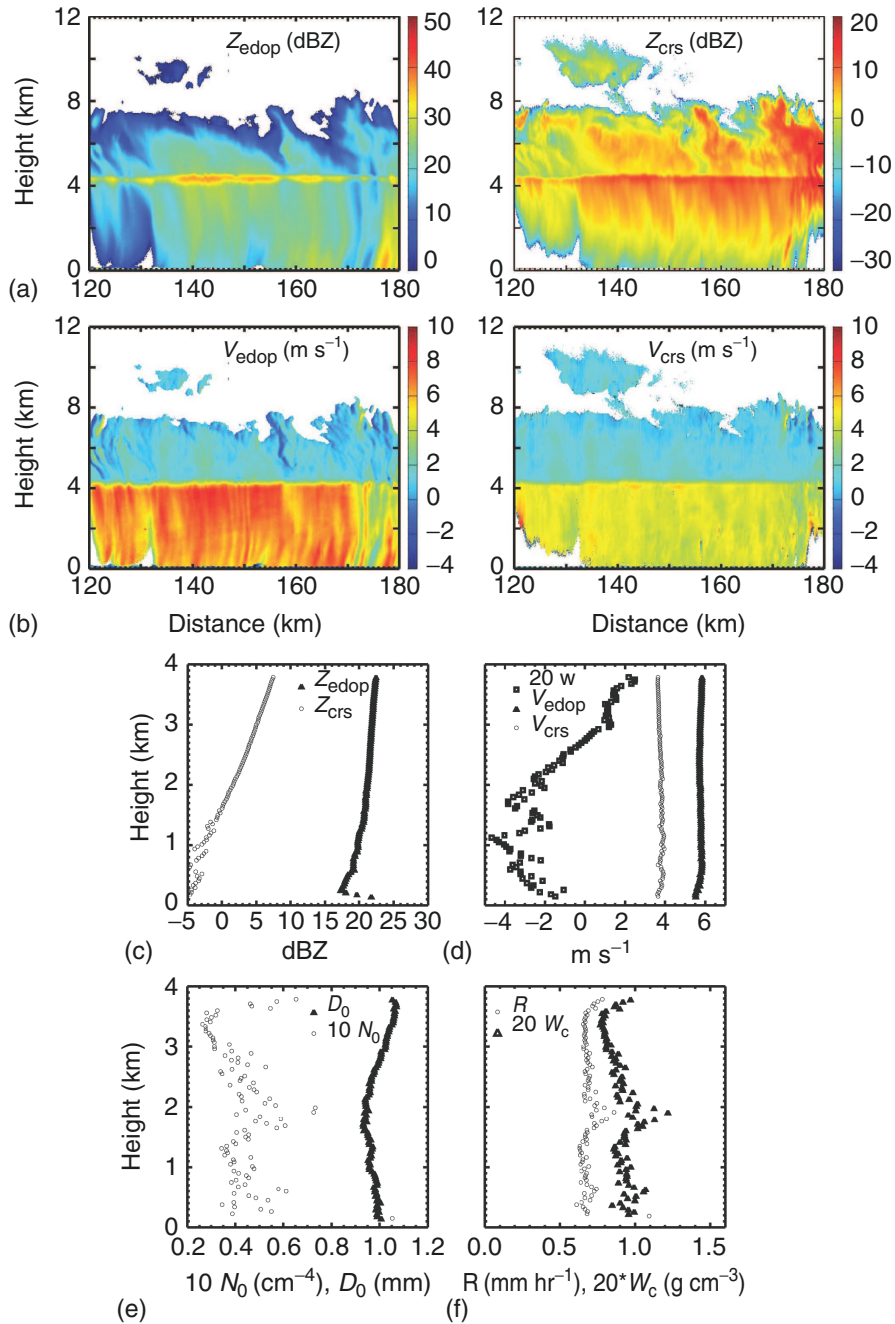


Figure A.13 Stratiform rain observed with EDOP (a) and CRS (b) in July 2002 over Florida (Tian, Heymsfield, Li and Srivastava, 2007: DOI: 10.1029/2006JD008144.). In the rain region below the melting band (4.3 km), scattering at 10 GHz is in the Rayleigh regime except for very large raindrops, whereas at 94 GHz, it is in the Mie regime except for the very small raindrops. The signal at 10 GHz is subject to little or no attenuation in light rain, while the signal at 94 GHz is subject to significant attenuation by rain and water vapor. Consequently, the mean Doppler velocity and reflectivity

measured at the two frequencies are quite different. These differences have been exploited to retrieve the parameters of an exponential raindrop size distribution, vertical air velocity, and attenuation by rain, melting band, and water vapor for the entire rain fields. Graphs (c–f) show the averages for the entire rain fields: reflectivity (c), velocity (d), median volume diameter, D_0 , and intercept parameter, N_0 , (e) rainfall rate R , and rain water content W (f). Source: Courtesy L. Tian and G. Heymsfield. To see a full-resolution image go to <[http:// ... /A13_edop.pdf](http://.../A13_edop.pdf)>.

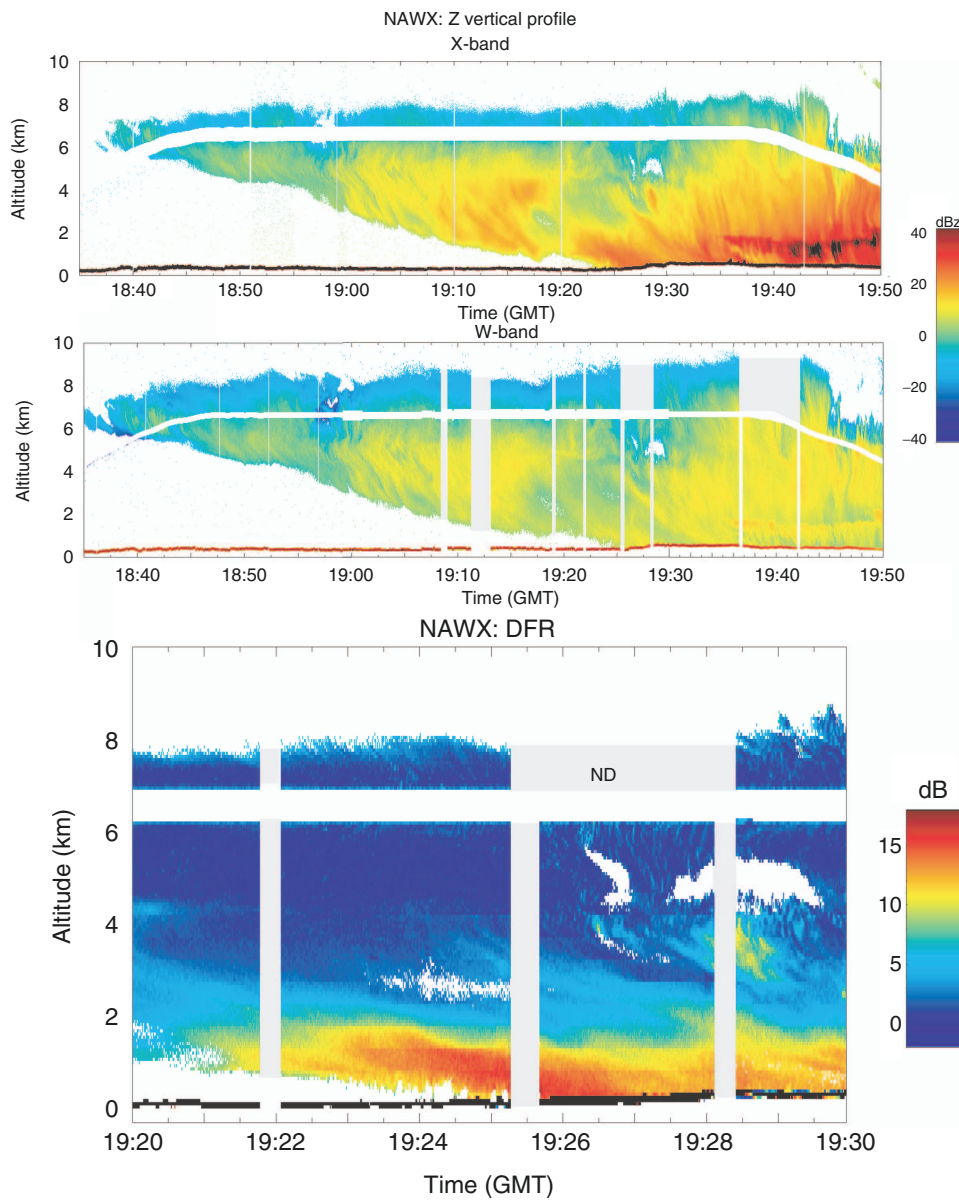


Figure A.14 During the C3VP campaign, the Convair flew in large winter storms over eastern Ontario on 1 March 2007. (a) and (b) show simultaneous measurements of W- and X-band reflectivity in vertical sections, respectively. (c) shows the difference between the two, showing values near 0 dB for regions, where ice crystals smaller than 1 mm were present (as per

in situ data); close to 5 dB for the regions above the melting band (~2 km altitude), where larger crystals and aggregates were detected; and a significant drop by up to 15 dB in the W-band signal in the rain below the melting band due to attenuation and resonance effects. *Source:* Courtesy of Mengistu Wolde. To see a full-resolution image go to <[http:// ... /A14_nawx.pdf](http://.../A14_nawx.pdf)>

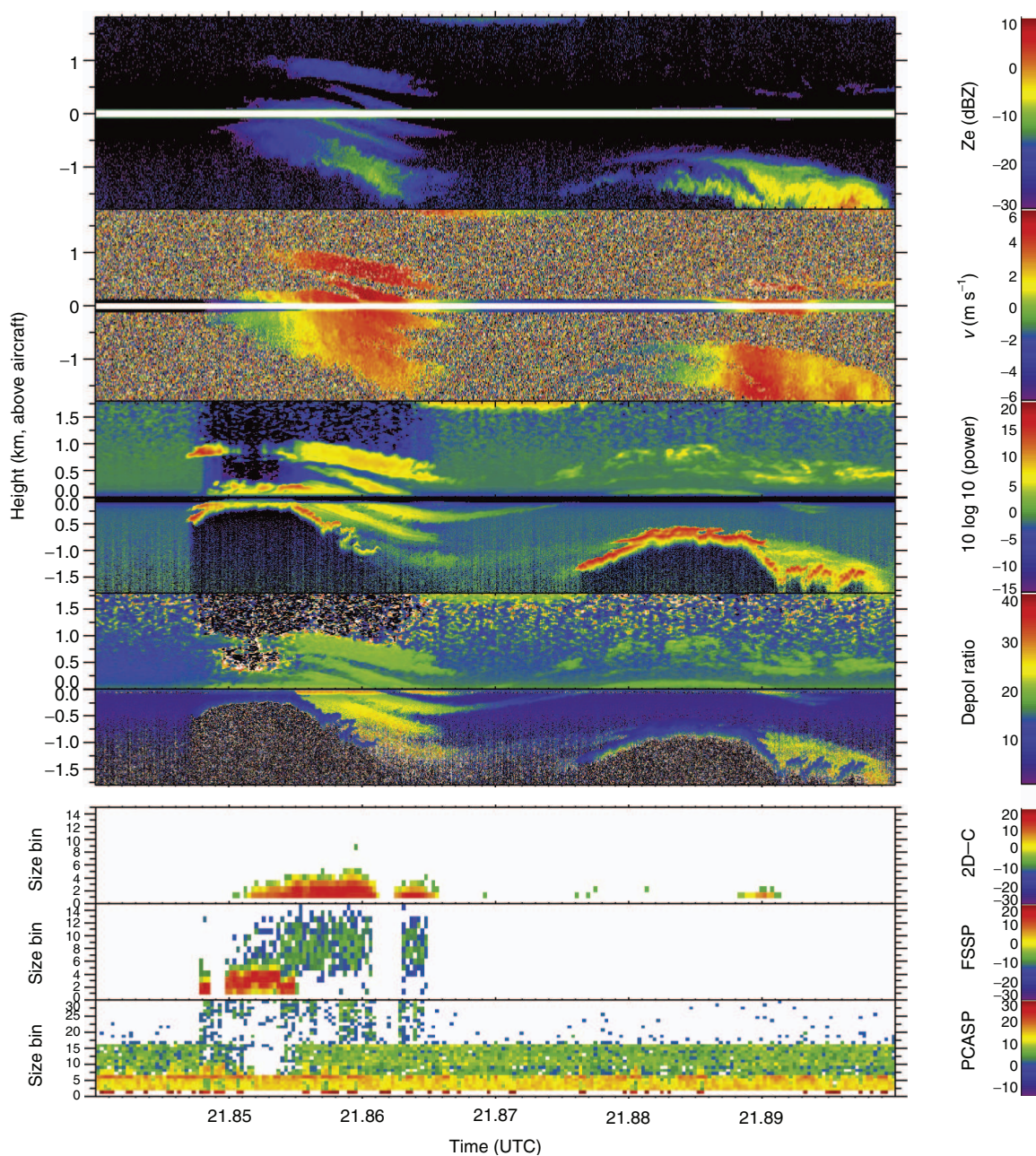


Figure A.15 RADAR (WCR), LIDAR (WCL), and *in situ* (Wyoming King Air) data collected in wave clouds. RADAR and LIDAR images are vertical sections combining data from upward and downward pointing beams. Wind direction is from left to right in the figure. The horizontal scale is ~ 3.6 km per major time tick of 0.01 h. The wave cloud on the left produced RADAR echoes only from its downwind side where ice crystals

are larger. The LIDAR return depicts the upwind part of this wave too. The polarization data from the lowest layer of this cloud indicates the presence of liquid water drops (low depol ratio). Similarly, almost all the wave on the right-hand side of the figure consisted of supercooled droplets. *Source:* Courtesy of Zhien Wang. To see a full-resolution image go to [http:// ... /A15_waico09.pdf](http://.../A15_waico09.pdf)

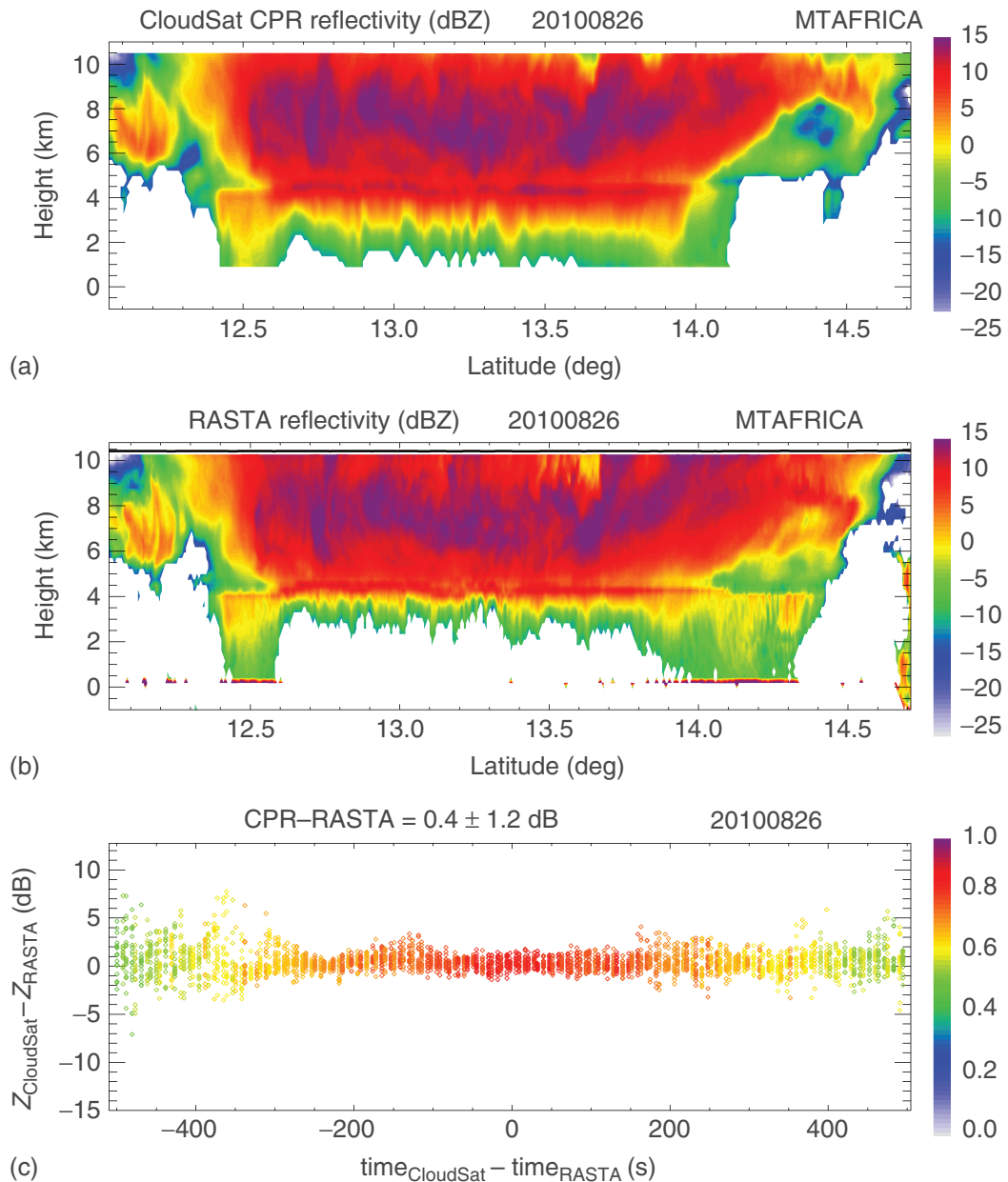


Figure A.16 Calibration check of the CloudSat CPR using the airborne cloud RADAR RASTA (Protat, *et al.* 2009). Flights below the track of CloudSat with airborne cloud RADARs are a unique and direct way of evaluating the instrument and cloud microphysics products from the CloudSat mission. Direct comparisons of the ocean backscatter (σ_0) indicate that on average, CloudSat measures ocean backscatter 0.4 ± 1 dB higher than the airborne cloud RADAR. (a) and (b) show collocated RASTA and CloudSat vertical cross sections through the stratiform part of a West-African squall line. (c) shows the difference as a function of

time lag between observations and of distance (color code). These data show that ice cloud reflectivities measured by CloudSat are 0.4 ± 1.2 dB higher than the airborne cloud RADAR. Both numbers are within the uncertainties in calibration of the airborne cloud RADARs, so the conclusion is that CloudSat is well calibrated. The results have been further confirmed using long time series of ground-based cloud RADAR observations and a statistical approach. *Source:* Courtesy of A. Protat and J. Delanoë. To see a full-resolution image go to <[http:// ... /A16_cpr-rasta.pdf](http://.../A16_cpr-rasta.pdf)>

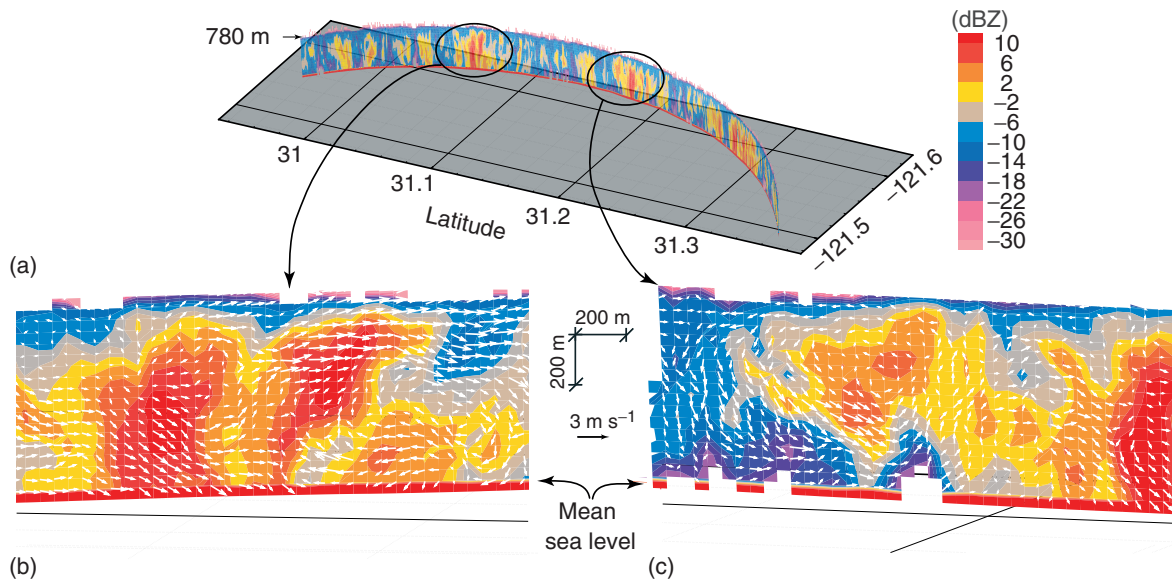


Figure A.17 Reflectivity and velocity measurements in marine stratus (Stevens *et al.*, 2003, DOI: 10.1175; BAMS-B4-5-579; Damiani and Haimov 2006, DOI: 10.1109; TGARS.2006.881745). Panel (a) depicts the reflectivity field between the aircraft flying above the cloud layer along a long arc at 780 m and the ocean surface. The presence of drizzle cells is evident. For two of

those cells, dual Doppler analysis of the 2D flow field is shown in panels (b) and (c), which identify convergence at the bases of updraft regions and reveal that the drizzle cells coincide with those updrafts. *Source:* Courtesy of R. Damiani, S. Haimov, and G. Vali. To see a full-resolution image go to <[http:// ... /A17_dycoms.pdf](http://.../A17_dycoms.pdf)>

```
# import thermodynamic module and rename to simplify usage
import egads.algorithms.thermodynamics as thermo

# get list of all NetCDF files in 'data' directory
filenames = egads.get_file_list('data/*.nc')

f = egads.input.EgadsNetCdf()
# create EgadsNetCdf instance

for name in filenames:
    # loop through files

        f.open(name, 'a')
        # open NetCdf file with append permissions

        Ts = f.read_variable('Tt')
        # read in static temperature
        Ps = f.read_variable('Ps')
        # read in static air pressure from file
```

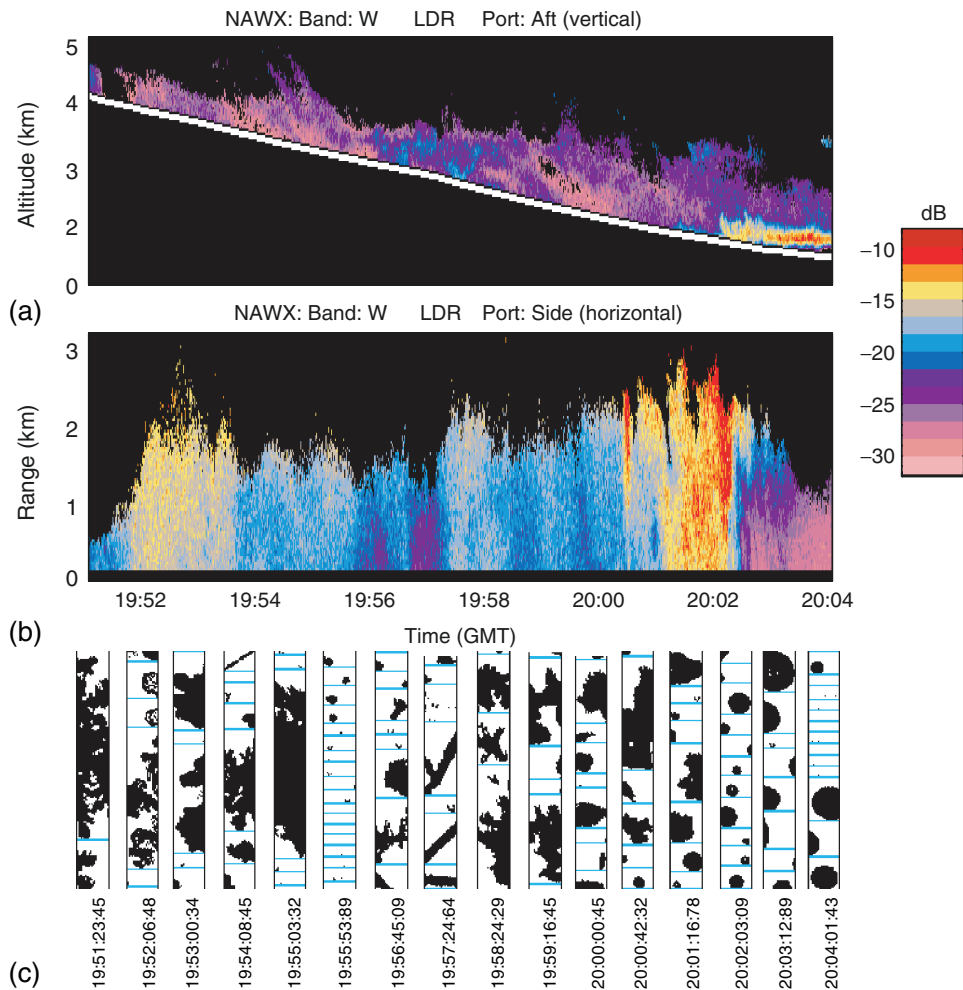


Figure A.18 LDR measured by NAWX on 1 March 2007 as the aircraft descended from an altitude of 4–1.5 km. (a) vertical cross section from upward pointing RADAR beam. The white line shows the aircraft altitude. (b) LDR from the side-looking dual-pol antenna. (c) sample of PMS 2D-C images corresponding to the aircraft altitude. *Source:* Courtesy M. Wolde. To see a full-resolution image go to [http:// ... /A18_ldr.pdf](http://.../A18_ldr.pdf).

```
rho = thermo.DensityDryAirCnrm().run(Ps, Ts)
# calculate density

f.write_variable(rho, 'rho', ('Time',))
# output variable

f.close()
# close file
```

For further usage information refer to the documentation included in the EGADS package. There are two sets of documentation. First, the EGADS Documentation that describes the use of the toolbox itself, including examples on how to explore the package from Python, an overview and examples of the file access classes, and a short sample processing script. Detailed descriptions of the

EGADS API are also included in this document. The second set of documentation – the EGADS Algorithm Handbook – describes each included algorithm in detail. This includes expected algorithm inputs and outputs, as well as a theoretical description and background of the algorithm itself and references to any relevant literature.

For questions and bug reports or to get more information, please contact eufarsp@eufar.net.